Czech Technical University in Prague
Faculty of Nuclear Sciences and Physical Engineering
Department of Physics

Study of non-linear evolution of the hadron structure within quantum chromodynamics

Master's thesis

Bc. Matěj Vaculčiak

Supervisor: Ing. Jan Čepila, PhD.

Prague, 2021

České vysoké učení technické v Praze
Fakulta jaderná a fyzikálně inženýrská
Katedra fyziky

Studium nelineární evoluce hadronové struktury v rámci kvantové chromodynamiky

Diplomová práce

Bc. Matěj Vaculčiak

Vedoucí práce: Ing. Jan Čepila, PhD.

Praha, 2021

Originální zadání DP

Declaration

I hereby declare that I have written this master's thesis independently and quoted all the sources of information used in accordance with methodological instructions on ethical principles for writing an academic thesis.

I have no reason to object to use this work according to the section 60 of Act No. 121/2000 Coll., On Copyright, on Rights Related to Copyright, and on Change of Some Acts (Copyright Act).

Prohlášení

Prohlašuji, že jsem svou diplomovou práci vypracoval samostatně a použil jsem pouze podklady uvedené v přiloženém seznamu.

Nemám žádný důvod proti použití tohoto školního díla ve smyslu § 60 Zákona č. 121/2000 Sb., o právu autorském, o právech souvisejících s právem autorským a o změně některých zákonů (autorský zákon).

In Prague, 2021 .....

Bc. Matěj Vaculčiak

Acknowledgement

I would like to express my gratitude towards my supervisor and the whole CTU group for their guidance, helpfulness and willingness to discuss all my nosy questions. My great gratitude also goes to my close ones, whose extensive support has always been a great encouragement for me.

Bc. Matěj Vaculčiak

Title:

Study of non-linear evolution of the hadron structure within quantum chromodynamics

Author: Bc. Matěj Vaculčiak

Field of study: Experimental Nuclear and Particle Physics

Thesis type: Master's thesis

Supervisor: Ing. Jan Čepila, PhD.

Abstract:

The subject of the hereby presented Master's Thesis is a study of the hadron structure, namely the parton saturation phenomenon present in the region of low Bjorken x in the deep-inelastic electron–proton scattering. A brief description of the experimental techniques utilised to study the hadron structure is presented followed by an introduction to theoretical models used to describe the underlying physics in terms of the proton structure functions.

Firstly, the parton model is described and an interpretation of the structure functions in terms of the parton distribution functions is explained. Subsequently, the emergent BFKL evolution equation is described and limitations of the model are examined. Secondly, the colour dipole picture is utilised to reformulate the scattering description in terms of the dipole scattering cross-section. Finally, the Colour Glass Condensate model is presented, utilising the colour dipole picture to overcome the parton model limitations by introducing the parton saturation phenomenon in form of the non-linear term of the Balitsky-Kovchegov (BK) equation.

Numerical solution of the BK equation is presented in 1 and 2 dimensions and theoretical predictions of observable quantities are given in comparison to experimental data collected at HERA, DESY.

Keywords: hadron structure, deep-inelastic scattering, parton saturation, colour dipole model, Colour Glass Condensate, Balitsky-Kovchegov evolution equation

Název práce:

Studium nelineární evoluce hadronové struktury v rámci kvantové chromodynamiky

Autor: Bc. Matěj Vaculčiak

Obor: Experimentální jaderná a částicová fyzika

Druh práce: Diplomová práce

Vedoucí práce: Ing. Jan Čepila, PhD.

Abstrakt:

Předmětem této diplomové práce je studium hadronové struktury, zejména pak jevu partonové saturace, který se projevuje při nízkých hodnotách Bjorkenova x v hluboce nepružném rozptylu elektronu na protonu. Jsou zde popsány jak experimentální techniky využívané při studiu hadronové struktury, tak teoretické modely používané k vysvětlení fyzikální podstaty procesů a to zejména v rámci tzv. protonových strukturních funkcí.

Prvním z modelů je tzv. partonový model, který interpretuje strukturní funkce pomocí partonových distribučních funkcí a evoluční BFKL rovnice. Vzhledem k limitacím partonového modelu je následně použit model barevného dipólu, který reformuluje popis hluboce nepružného rozptylu pomocí dipólové rozptylové amplitudy. Její zkoumání je předmětem Colour Glass Condensate modelu, který v rámci jejího popisu zavádí jev partonové saturace, konkrétně ve formě nelineárního členu tzv. Balitsky-Kovchegov evoluční rovnice, čímž zároveň překonává zmíněné limitace partonového modelu.

Závěrem jsou prezentována numerická řešení Balitsky-Kovchegov rovnice a to postupně v jedné a dvou proměnných. Tato jsou pak využita k výpočtu teoretických předpovědí pozorovatelných veličin a jejich porovnání s experimentálně naměřenými daty na urychlovači HERA, DESY.

Klíčová slova: hadronová struktura, hluboce nepružný rozptyl, partonová saturace, model barevného dipólu, Colour Glass Condensate, Balitsky-Kovchegov evoluční rovnice

Contents

Chapter 1

Introduction

Although ordinary (baryonic) matter forms merely 4.9% of the total content of our universe [1], it is the only component we are in direct contact with and from which we consist. This is a strong enough motivation to focus on the study of not only baryons, but hadrons in general.

Hadrons are the building blocks of ordinary matter. As described in Chapter 2, they are composite objects consisting of elementary quarks which are held together by gluons, the strong interaction mediators. Similar to the electric charge defining the strength of electromagnetic interaction, the strong interaction is defined by the so-called colour charge. The aforementioned quarks and gluons are the only elementary carriers of this colour charge and therefore the only strongly interacting particles.

To form stable objects, the quarks form colour neutral hadrons. Based on the number of the constituent (valence) quarks, hadrons are categorised as either:

1. mesons, consisting of a quark-antiquark pair,

2. baryons, consisting of three quarks or three antiquarks.

The only truly stable[2] hadron is the proton and will therefore be the main subject of investigation within this thesis.

Historically, the proton was first discovered by Ernest Rutherford in 1919 [2] when shooting alpha particles against nitrogen gas. In the 1960s, high energy electron beams were fired at protons at SLAC[3], suggesting that the proton is not elementary, but point-like scattering centres are present within [3]. The

[1] According to the latest Planck results [1]. The rest of the universe is then formed by dark energy ($\sim 68.5\%$) and dark matter ($\sim 26.5\%$).

[2] Proton is the only hadron that has not yet been seen to decay. Neutrons can be considered stable when part of a nucleus, however, free neutrons decay after ~ 15 minutes.

[3] The Stanford Linear Accelerator Center.

quark model then identified the proton as a collective state of two up quarks and a down quark.

One of the most significant features of quantum chromodynamics (QCD), which describes strong interaction, are its mediators. Unlike the photons in quantum electrodynamics (QED), gluons interact with themselves which means that, e.g. a high-energy (hard) gluon can radiate a lower-energy (softer) one.

Taking this into account, the historical description of hadrons as a collection of two or three valence quarks, suddenly became over-simplistic. Many secondary (so-called sea) quarks and gluons emerge in a hadron as its energy rises. Thus, a complex energy-dependent structure emerges (as artistically depicted in Fig. 1.1), which needs to be understood.

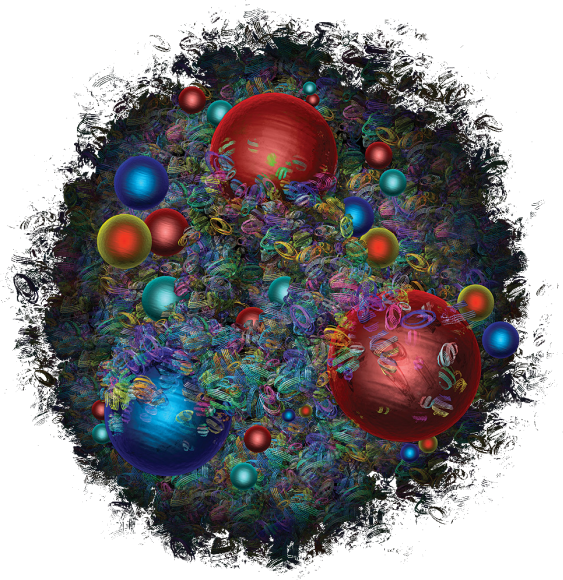

Fig. 1.1: An artistic visualisation of the proton content as presented in CERN Courier. The valence quarks are depicted as the large red (up quarks) and blue (down quark) spheres [4].

Reaching even higher collision energies, the regime of deep-inelastic electron–proton scattering (DIS) was reached. The cross section of such a process encodes the information about the proton structure in the form of the so-called structure functions $F(x, Q^2)$. They depend on two variables, commonly the Bjorken x and virtuality Q^2 are chosen, corresponding to various evolutions as shown in Fig. 1.2.

Having fixed x and varying the virtuality, the energy (and therefore the wavelength) of the virtual photon[4] varies. For large Q^2 values, the wavelength

[4]Virtual photon is the leading mediator of the deep-inelastic scattering.

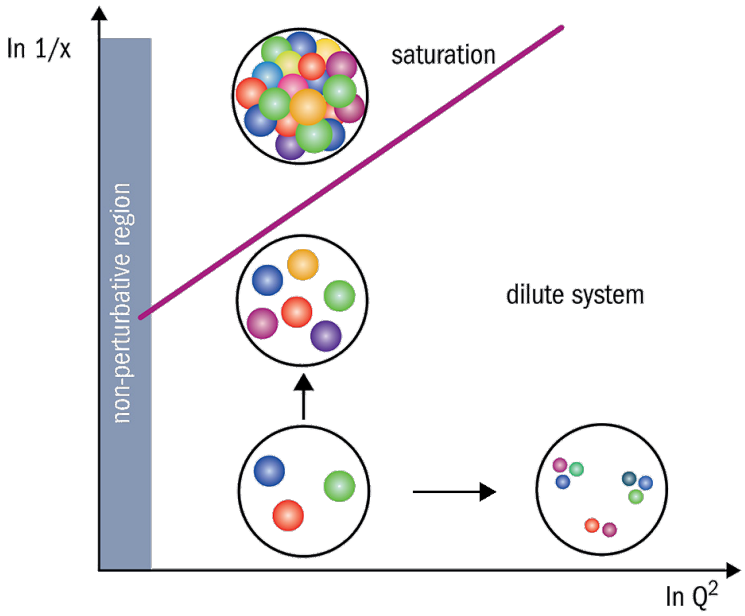

Fig. 1.2: A diagrammatic representation of the two possible evolution directions of the proton structure [5]. The horizontal direction is described by the DGLAP evolution equations, the first step of the vertical direction corresponds to the BFKL evolution and the second one is given by the JIMWLK equations (or an approximation to them: the BK equation).

decreases and smaller objects can be probed as indicated by the horizontal arrow in Fig. 1.2.

On the other hand, having the virtuality fixed and examining the region of low x corresponds to studying the low energy components of the proton structure as indicated by the vertical arrow. The lower the x, the more (low energy) particles are found.

A very successful model in terms of giving a phenomenological explanation of the structure functions is the parton model suggested by Richard Feynman in 1969 [6, 7]. It interprets them in terms of parton[5] distribution functions (PDFs) defining the probability density of finding a parton with a particular fractional energy in the proton. The evolution of the PDFs (and therefore the structure functions) with respect to the virtuality (the horizontal axis of Fig. 1.2) is driven by the DGLAP evolution equations [8]. The vertical axis corresponds to the evolution in the Bjorken x. The first step (in relatively large values of x) is given by the BFKL equation while the region of low x is described by the BK equation, which is the main point of interest in this thesis.

[5]Within the model, parton is a general term for proton constituents: quarks and gluons.

Although the BFKL evolution satisfyingly describes the currently available experimental data, there are both theoretical and phenomenological limitations for the kinematic regions not yet reached. The theoretical limit is given by the Froissart bound [9] which puts a restriction on the growth of the cross section with respect to the centre-of-mass energy. Phenomenologically, the problem with the BFKL evolution can be tracked to its linearity which does not allow for incorporating any recombination mechanism. In other words, according to the BFKL equation a parton (namely gluon) can split into two partons with lower energy, but two low-energy partons can not recombine into one. This way, an infinite number of partons with infinitely small energy (low-x region) would appear in a proton.

To deal with this problem, two steps are taken. Firstly, the electron–proton collision is viewed in the so-called colour dipole picture as described in Chapter 3. Here the virtual proton is understood to split into a quark-antiquark pair (a colour dipole) and this dipole is the subject of interaction with the proton. In this case, the cross section is described by the so-called dipole scattering amplitude N. In the second step (described in Chapter 4), an effective theory, the Colour Glass Condensate, is presented, giving an infinite set of the JIMWLK equations to predict the evolution of the dipole scattering amplitude with respect to the Bjorken x.

Unfortunately, due to their complexity, there is no known analytical solution to the JIMWLK equations. However, as a limit case, it is possible to separate the so-called Balitsky-Kovchegov (BK) equation which is simpler to solve numerically and presents an improvement of the BFKL evolution by introducing a non-linear term. This term accounts for a parton (namely gluon) recombination and therefore solves the aforementioned problem of the BFKL equation.

Besides the rapidity[6] Y dependence, the dipole scattering amplitude $N(\vec{r}, \vec{b}, Y)$ depends on two 2-dimensional vectors $\vec{r}$ and $\vec{b}$ representing the colour-dipole size and the collision impact parameter, respectively. The full BK equation is therefore considered as 4-dimensional. The state-of-the-art BK equation solutions have yet regarded only 2 dimensions (the dipole size $|\vec{r}|$ and impact parameter size $|\vec{b}|$) in the numerical calculation.

Besides an introduction to the general problematics described above, the presented thesis aims to show both the 1-D and 2-D solutions of the BK equation in Chapter 5, together with the resulting theoretical predictions of the observable quantities in Chapter 6, namely the F_2 structure function and the so-called reduced cross section σ_r.

[6]The dipole scattering amplitude is formulated in terms of rapidity Y which is directly connected to the Bjorken x. Therefore, the Y-evolution of N corresponds to the x-evolution of the DIS cross section.

Chapter 2

Hadron structure investigation

The current way to study the hadron structure is by considering a deep-inelastic scattering (DIS). Such experiments were conducted at, e.g. HERA[1] [10]. Other important experimental processes are the ultra-peripheral collisions at LHC[2] [11].

The specific hadron whose structure is the subject of investigation within this work (and most of the current experiments) is a the proton. The reason is quite straightforward; it is the only stable hadron we are able to effectively physically manipulate; accelerate and lead to collisions at sufficiently high energies.

Now, the ideal particle, in the sense of investigating the proton structure by collision, is the electron or its antiparticle the positron[3]. There are other ways in which a proton can take part in a collision; it can be shot at a fixed target, collide with another proton, or even be a constituent of heavier-nuclei collisions. However, none of these provide sufficiently clean information about the proton itself. Electrons and positrons, on the other hand, are, as far as we know, elementary (non-composite) particles, so focusing on the electron–proton collisions where the electron is present in both the initial and final states, enables one to maximise the information gained on proton structure.

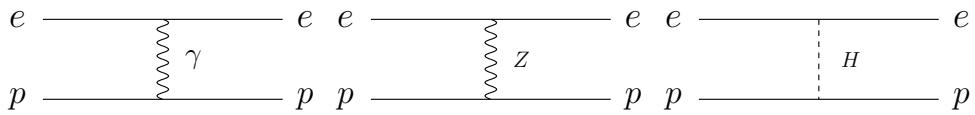

(a) single γ exchange (b) single Z exchange (c) single Higgs exchange

Fig. 2.1: Possible neutral channels mediating an electron–proton interaction.

[1] A particle accelerator at Deutsches Elektronen-Synchrotron (DESY) colliding hadrons with leptons.

[3] Positrons can be equivalently used in the experiments investigating proton structure. However, for the notation simplicity, only electrons will be mentioned in the rest of this chapter.

The aforementioned interaction can be either mediated by some neutral channel, so that an electron is still present in the final state, or a charged channel, where the electron turns into a positron. Taking into account the leading order perturbation theory, there are 3 elementary objects to possibly mediate such an interaction: the photon, the Z boson, and the Higgs boson. Diagrams of such processes are shown in Fig. 2.1.

The main difference[4] between the cross sections of such processes lies in the propagators of the particular mediators:

$$\sigma_\gamma \sim \left(\frac{1}{q^2}\right)^2, \tag{2.1}$$

$$\sigma_Z \sim \left(\frac{1}{q^2 - M_Z^2}\right)^2, \tag{2.2}$$

$$\sigma_\gamma \sim \left(\frac{1}{q^2 - M_H^2}\right)^2. \tag{2.3}$$

In this work, the kinematic range of interest[5] corresponds to $-q^2$ ranging from a few to hundreds of GeV^2. Within this range, the single photon exchange is clearly dominant by more than 4 orders of magnitude.[6] The other cross-sections are suppressed by the fourth power of the boson masses; $M_Z \approx 91.2$ GeV and $M_H \approx 125.1$ GeV.

2.1 Deep-inelastic scattering

Having a fully fixed initial state (electron colliding with a proton) and a partially fixed final state (containing an electron), there are several experimental regimes to be distinguished with respect to the proton's final state. They are denoted as *elastic*, *inelastic*, and *deep-inelastic scattering*.

The *elastic scattering* describes a process where the electron simply scatters off the proton which remains intact, as shown in Fig. 2.2. This way the final state consists again of a proton and an electron.

The elastic scattering is the dominant process at lower exchanged energies and its differential cross section is described by the (covariant [12]) Rosenbluth formula [8, 13, 14]

$$\frac{\mathrm{d}\sigma}{\mathrm{d}Q^2} = \frac{4\pi\alpha_{em}^2}{Q^4}\left[\left(1 - y - \frac{m_p^2 y^2}{Q^2} f_2(Q^2)\right) + \frac{1}{2} y^2 f_1(Q^2)\right]. \tag{2.4}$$

[4] Neglecting the role of different vertex factors.

[5] The kinematic range is connected to the validity range of the Balitsky-Kovchegov equation whose description is subject to Chapter 4.

[6] The same argumentation would follow if a positron was taken into account as a part of the final state. The propagator of the charged W boson mediating the interaction is suppressed by the boson's mass ($M_W \approx 80.4$ GeV) just like in the case of the Z exchange.

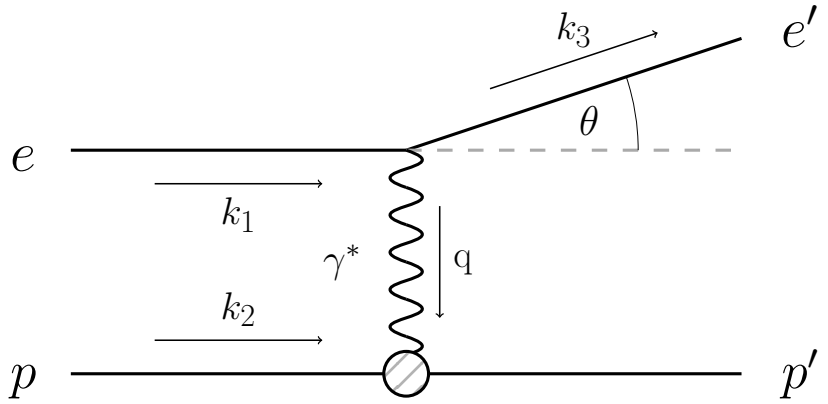

Fig. 2.2: A schematic representation of an electron–proton elastic scattering. The electron with momentum k_1 scatters off the proton with momentum k_2 by exchanging a virtual photon with momentum q. The post-collision electron is deflected from its initial direction by angle θ and carries momentum k_3. In case of the ideally elastic scattering, the proton momentum remains unchanged.

Here α_{em} is the electromagnetic coupling constant and m_p corresponds to the proton mass.

The variable y is a dimensionless Lorenz-invariant quantity referred to as *inelasticity*. It is defined as

$$y := \frac{k_2^\mu q_\mu}{k_2^\mu k_{1\mu}} \tag{2.5}$$

and in the rest frame of the proton

$$k_1 = \begin{pmatrix} E_1 \\ 0 \\ 0 \\ E_1 \end{pmatrix}, \quad k_2 = \begin{pmatrix} m_p \\ 0 \\ 0 \\ 0 \end{pmatrix}, \quad k_3 = \begin{pmatrix} E_3 \\ E_3 \sin(\theta) \\ 0 \\ E_3 \cos(\theta) \end{pmatrix}, \tag{2.6}$$

it can be expressed as

$$y = 1 - \frac{k_2^\mu k_{3\mu}}{k_2^\mu k_{1\mu}} = 1 - \frac{E_1}{E_3}, \tag{2.7}$$

which corresponds to one minus the fraction of the energy lost by the electron in the scattering process. As mentioned earlier, the elastic scattering dominates at low exchanged energies, therefore the lower the y, the more elastic the scattering, hence the name *inelasticity*.

The definition of the remaining variable, *virtuality*,

$$Q^2 := -q^2, \tag{2.8}$$

is straightforward. The reason for its introduction is that for high energies[7], the electron mass can be neglected,

$$Q^2 = -(k_1 - k_3)^2 = -2m_e^2 + 2E_1E_3 - 2k_1k_3\cos(\theta) \approx 2E_1E_3(1 - \cos(\theta)), \tag{2.9}$$

implying that, unlike q^2, the virtuality Q^2 is always positive.

Finally, the f functions reflect the composite nature of the proton, namely, its purely magnetic contribution in $f_1(Q^2)$ and a mixture of magnetic and electric contributions in $f_2(Q^2)$.

Reaching sufficiently high collision energies, the proton can be disintegrated by the collision. This results in a final state of an electron and secondary particles emerging from the shattered proton, denoted as X in Fig. 2.3. This is the aforementioned *inelastic scattering*.

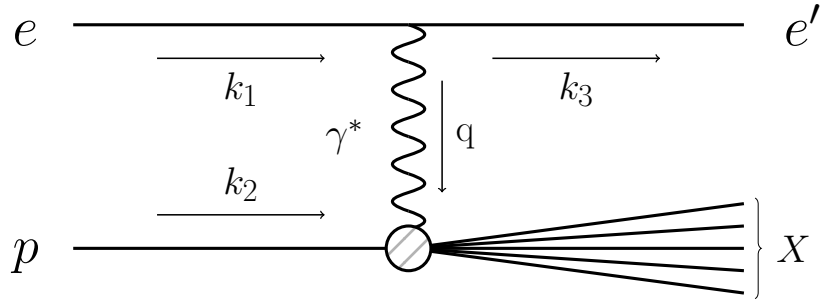

Fig. 2.3: A schematic representation of an electron–proton inelastic scattering. The electron with momentum k_1 scatters off the proton with momentum k_2 by exchanging a virtual photon with momentum q. The post-collision electron carries momentum k_3 and the proton is shattered giving rise to secondary particles denoted by X.

An extra degree of freedom in the form of an unspecified state of the secondary particles is reflected in the transition from a single[8] to a double differential cross section. Its full form reads [12, 13]

$$\frac{\mathrm{d}^2\sigma}{\mathrm{d}x\mathrm{d}Q^2} = \frac{4\pi\alpha_{em}^2}{Q^4}\left[\left(1 - y - \frac{m_p^2y^2}{Q^2}\right)\frac{F_2(x,Q^2)}{x} + y^2F_1(x,Q^2)\right]. \tag{2.10}$$

Up to two main features, its form is very similar to the covariant Rosenbluth formula (2.4).

Firstly, a new dimensionless Lorenz-invariant quantity x is presented. It is the so-called *Bjorken x* defined as

$$x := \frac{Q^2}{2p_2^\mu q_\mu} \tag{2.11}$$

[7] Mainly valid for inelastic scattering.

[8] In case of an elastic scattering.

and gets a very particular interpretation within the parton model.

The second important feature is the transition from the functions $f_1(Q^2)$, $f_2(Q^2)$ to $F_1(x, Q^2)$ and $F_2(x, Q^2)$. These are referred to as proton *structure functions* and are the key object to measure and analyse in order to learn about the hadronic structure. Similarly to the Bjorken x, the explanation comes from the interpretation within the parton model.

The *deep-inelastic scattering* is defined as a limit case of the inelastic scattering where $Q^2 >> m_p^2 y^2$. This reduces (2.10) to [12]

$$\frac{\mathrm{d}^2\sigma}{\mathrm{d}x\mathrm{d}Q^2} = \frac{4\pi\alpha_{em}^2}{Q^4}\left[(1-y)\frac{F_2(x,Q^2)}{x} + y^2 F_1(x,Q^2)\right]. \tag{2.12}$$

Taking this limit makes it possible to simplify the measurement and analysis of the electron–proton collision data, allowing one to focus on the study of the structure functions.

Being able to predict the structure functions corresponds to a level of understanding in the composition of hadrons. Therefore, it is also one of the main goals of this work to present predictions of the proton structure functions and compare them with experimental data.

2.2 The parton model

In order to describe the deep-inelastic electron–proton scattering and interpret the structure functions, *the parton model* was proposed by Richard Feynman in 1969 [6, 7]. It suggests that protons consist of generic[9] spin-half point-like objects, which are supposed to be essentially free within the hadron.

Since, at the time, the idea of quarks and gluons was not yet generally accepted [12], these elementary constituents were termed *partons*.

Instead of an interaction between the photon and the hadron as a whole, the deep-inelastic scattering is then interpreted as an elastic scattering of the electron off one of the partons as depicted in Fig. 2.4.

The formulation of the parton model works within the concept of the *infinite momentum frame*. There are two main defining assumptions:

1. the proton mass is negligible with respect to the full proton energy[10]

$$m_p << E_2 = p_2 \Rightarrow k_2 = \begin{pmatrix} E_2 \\ 0 \\ 0 \\ E_2 \end{pmatrix}, \tag{2.13}$$

[9] In today's terminology a parton is a general term for both quarks and gluons.

[10] Keeping the notation of Chapter 2.

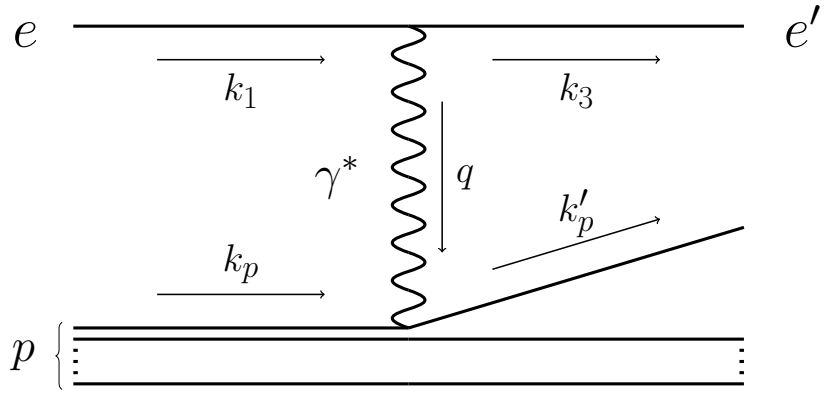

Fig. 2.4: A schematic representation of the parton-model interpretation of the electron–proton inelastic scattering. The electron with momentum k_1 scatters off a parton inside the proton with momentum k_p by exchanging a virtual photon with momentum q. The post-collision electron carries momentum k_3 and the struck parton has momentum k'_p.

2. the transverse momentum of the struck parton (see Fig. 2.4) can be neglected and its 4-momentum reads

$$k_p \equiv \xi k_2 = \begin{pmatrix} \xi p_2 \\ 0 \\ 0 \\ \xi p_2 \end{pmatrix}, \tag{2.14}$$

where ξ represents the fraction of the proton energy carried by the parton.

As seen in Fig. 2.4, the 4-momentum of the struck parton after the collision is

$$k'^{\mu}_p = k^{\mu}_p + q^{\mu}. \tag{2.15}$$

Squaring the relation yields

$$m_p^2 = m_p^2 + 2\xi p_2 q + q^2 \;\Rightarrow\; \xi = \frac{-q^2}{2p_2 q} = \frac{Q^2}{2p_2 q} = x, \tag{2.16}$$

where the last equality uses the definition of the Bjorken x in Eq. (2.11). Hence, it is clear that the interpretation of the Bjorken x within the parton model is that it represents the fractional momentum carried by the parton engaging in the deep-inelastic scattering.

As the partons are supposed to interact with each other, they continuously redistribute the full hadron momentum. Therefore, they need to be approached statistically. For this purpose, the *parton distribution functions* (PDFs) $f_j(x, Q^2)$ are presented [12]. They represent the number density of

a j-type parton[11] with a particular momentum given by the Bjorken x at a scale Q^2, so that

$$f_j(x, Q^2)\mathrm{d}x \tag{2.17}$$

corresponds to the number of j-type partons with fractional momentum between x and $x + \mathrm{d}x$.

To keep the correspondence to the idea of the proton consisting of two up quarks and one down quark, the so-called valence quark distributions are separated out of the total PDFs, as seen in the measurements in [15].

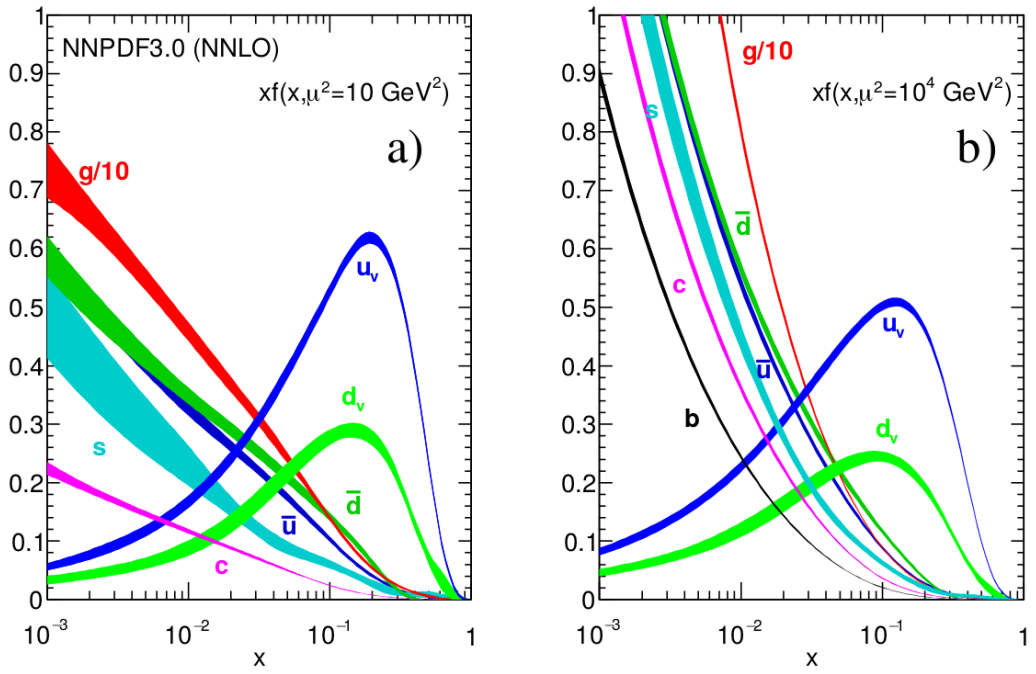

Fig. 2.5: The coloured bands represent x times the unpolarized parton distributions $f_j(x, \mu^2)$, where $f_j = u_v, d_v, u, d, s \cong \bar{s}, c \cong \bar{c}, b \cong \bar{b}, g$ [15]. The energy scale is denoted by μ^2.

Initially, the parton model viewed DIS as an elastic electron–fermion scattering. The cross section of such a process is given (neglecting the parton mass) by [12]

$$\frac{\mathrm{d}\sigma}{\mathrm{d}Q^2} = \frac{4\pi\alpha_{em}^2}{Q^4}\left[(1-y) + \frac{y^2}{2}\right]e_j^2, \tag{2.18}$$

where e_j is the fermion electric charge.

[11] Identifying partons with quarks and gluons, the index j denotes gluons or the quark and antiquark flavours, $j \in \{g, u, \bar{u}, d, \dots\}$.

Summing over all partons, we get a double differential DIS cross section in the form

$$\frac{\mathrm{d}^2\sigma}{\mathrm{d}x\mathrm{d}Q^2} = \frac{4\pi\alpha^2}{Q^4}\left[(1-y)+y^2\right]\sum_j e_j^2 f_j(x). \tag{2.19}$$

Comparing with Eq. (2.12), we see that

$$F_2(x,Q^2) = 2xF_1(x,Q^2) = x\sum_j e_j^2 f_j(x). \tag{2.20}$$

In the sense of the PDFs, the second equation gives a direct phenomenological interpretation of the structure functions, while the first part predicts the so-called Callan-Gross relation, which, to a certain extent, agrees with the observed data. The relation is not exact, as the parton model approximates partons as fermions[12], and a correction to the relation in the form of $F_L(x,Q^2)$ is given in Eq. (3.11).

For the limit of low x and finite and fixed Q^2, the Balitsky-Fadin-Kuraev-Lipatov (BFKL) equation has been derived [16, 17] to give a theoretical prediction of the low-x gluon density function. The leading logarithmic approximation[13] reads

$$\frac{\partial\varphi(x,k_T^2)}{\partial\ln(1/x)} = \frac{3\alpha_s}{\pi}k_T^2\int_0^\infty \frac{\mathrm{d}k_T'^2}{k_T'^2}\left[\frac{\varphi(x,k_T'^2)-\varphi(x,k_T^2)}{|k_T'^2-k_T^2|}+\frac{\varphi(x,k_T^2)}{\sqrt{4k_T'^4+k_T^4}}\right]. \tag{2.21}$$

The variable k_T represents the transverse gluon momentum and α_s is the strong coupling.

The function $\varphi(x,k_T^2)$ is the so-called unintegrated gluon density, connected to the gluon distribution function $g(x,Q^2)$ by

$$xg(x,Q^2) = \int_0^{Q^2}\frac{\mathrm{d}k_T^2}{k_T^2}\varphi(x,k_T^2). \tag{2.22}$$

As described in Ref. [9], unitarity implies a constraint on scattering amplitudes leading to the so-called Froissart bound. It limits the possible theoretical growth of cross-sections as

$$\sigma(s) < A\ln^2(s), \tag{2.23}$$

where s is the centre-of-mass energy squared and $A \sim 60$ mb is a constant determined from the pion mass [9].

[12] Electrically neutral gluons are not taken into account in Eq. (2.18).

[13] Its region of validity is $\alpha_s(Q^2)\ln\frac{Q^2}{Q_0^2} << \alpha_s(Q^2)\ln\frac{1}{x} \lesssim 1$ [16].

Unfortunately, the fast growth of the PDFs at low x (see Fig. 2.5) leads to a violation of the Froissart bound.

It can be seen by focusing on the most violently divergent gluon distribution. The BFKL equation predicts a power-like growth of the unintegrated gluon density at small x [17]

$$\varphi(x, k_T^2) \sim \left(\frac{1}{x}\right)^{\frac{4\alpha_s N_C}{\pi^2} \ln 2}, \tag{2.24}$$

as the BFKL evolution does not contain any mechanism of saturation. The number of colours is denoted by N_C and α_s is the strong coupling.

The parton (namely gluon) saturation can be obtained within more complex models such as the Colour Glass Condensate described in Chapter 3.

Chapter 3

The colour dipole model of DIS

An alternative way to describe the deep-inelastic electron–proton scattering and obtain a theoretical prediction of the structure functions is the *colour dipole model* [9, 18–21].

To incorporate the essence of the strong interaction in the inelastic electron–proton scattering, the underlying interaction of the virtual photon with the proton is further investigated, while neglecting the role of the electron.

Using the Fock expansion of the virtual photon wave function, the photon is taken to fluctuate into the colour dipole, which is its simplest[1] strongly-interacting Fock state. This colour dipole is then the subject of the interaction with the proton, as shown in Fig. 3.1.

In the proton rest frame, the dipole lifetime is much longer[2] than the timescale on which the interaction with the proton happens [20]. The γ^*-p interaction can be, therefore, considered to happen in two steps:

1. the virtual photon fluctuates into the colour dipole,

2. the colour dipole interacts with the proton.

The cross section for the interaction between the proton and a longitudinally (L) or a transversely (T) polarised photon is then given by [20, 22]

$$\sigma_{T,L}^{\gamma^* p}(x, Q^2) = \sum_f \int \mathtt{d}^2\vec{r} \int_0^1 \mathtt{d}z |\Psi_{T,L}^{(f)}(\vec{r}, Q^2, z)|^2 \sigma_{q\bar{q}}(\vec{r}, \tilde{x}_f), \tag{3.1}$$

where the $|\Psi_{T,L}(\vec{r}, z)|^2$ term corresponds to the γ-to-$q\bar{q}$ fluctuation, and the $\sigma_{q\bar{q}}(\vec{r}, \tilde{x})$ term describes the dipole-proton interaction.

[1] A gluon can not interact directly with a photon. Quarks can, but are charged, so at least two are needed to form an electrically neutral and colour neutral object.

[2] This assumption is valid for low x, namely under the condition $x << \frac{1}{m_p r_p}$, where the m_p is the proton mass and the r_p is the proton radius.

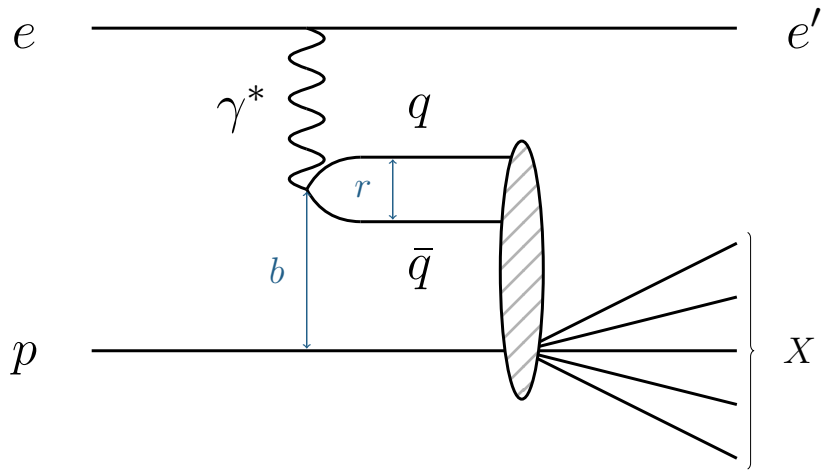

Fig. 3.1: A schematic representation of an electron–proton elastic scattering in the colour dipole model. The virtual photon mediating the interaction splits into a quark-antiquark dipole of size r which then interacts with the proton at an impact parameter b, .

The variable Q^2 is the virtuality defined in (2.9). On the right-hand side, the only Q^2-dependent object is the photon wave function $\Psi_{T,L}^{(f)}(\vec{r}, Q^2, z)$. However, certain dependence is also present in the $\sigma_{q\bar{q}}(\vec{r}, \tilde{x})$ in form of the $\tilde{x}$ variable defined as

$$\tilde{x}_f := x\left(1 + \frac{4m_f^2}{Q^2}\right). \tag{3.2}$$

Here x is the Bjorken x from (2.11) and m_f represents the mass of a quark with flavour f. The necessity of the $\tilde{x}$ definition is connected to approaching the photoproduction limit [19].

The two-dimensional[3] vector $\vec{r}$ represents the transverse size of the colour dipole as shown in Fig. 3.1. The variable z represents the fraction of the photon light-cone momentum [23] carried by the emerging quark. The antiquark then carries the fractional momentum $(1 - z)$.

As shown later in this chapter, the photon–proton cross section can be used to calculate the F_2 and F_L structure functions and therefore the cross section of the whole deep-inelastic electron–proton scattering.

The probability of the virtual photon splitting into the colour dipole, or equivalently the squared virtual photon wave function, can be calculated within the formalism of light-cone quantum field theory as shown in [24, 25]. The square of the transversally and longitudinally polarised wave functions summed

[3] A rotational symmetry of the interaction is assumed with respect to the dipole ===momentum as an axis.

over spin and polarisation is given by [19]

$$|\Psi_T^{(f)}(\vec{r},Q^2,z)|^2 = \frac{3\alpha_{em}}{2\pi^2}e_f^2\{[z^2+(1-z)^2]\epsilon_f^2K_1^2(\epsilon_f r)+m_f^2K_0(\epsilon_f r)\}, \quad (3.3)$$

$$|\Psi_L^{(f)}(\vec{r},Q^2,z)|^2 = \frac{3\alpha_{em}}{2\pi^2}e_f^2\{4Q^2z^2(1-z)^2K_0^2(\epsilon_f r)\}. \quad (3.4)$$

Here, α_{em} is the fine electromagnetic coupling. The summation is carried out over the quark flavours f where e_f is the electric charge of the respective quark. The functions $K_0(\epsilon_f r)$ and $K_1(\epsilon_f r)$ are the modified Bessel functions of the second kind. The variable ϵ_f is defined as

$$\epsilon_f^2 := z(1-z)Q^2 + m_f, \quad (3.5)$$

where m_f is the quark mass.

The cross section of the interaction between the proton and the colour dipole is given by [9]

$$\sigma_{q\bar{q}}(\vec{r},\tilde{x}) \equiv 2\int \mathrm{d}^2\vec{b}N(\vec{r},\vec{b},Y). \quad (3.6)$$

The newly presented quantity $N(\vec{r},\vec{b},Y)$ is the dipole amplitude. By the optical theorem, it is connected to the invariant amplitude of the dipole–proton scattering as its imaginary part [20], but most importantly it can be calculated within the Colour Glass Condensate model from the Balitsky-Kovchegov equation.

The two-dimensional vector $\vec{b}$ represents the impact parameter of the dipole-proton collision as depicted in Fig. 3.1. In the earlier models[4], the $\vec{b}$ dependence was integrated out as a mere fit parameter σ_0

$$\sigma_{q\bar{q}}(\vec{r},\tilde{x}) \approx \sigma_0 N(\vec{r},Y). \quad (3.7)$$

However, within this work the $\vec{b}$ dependence is considered as a part of the BK evolution equation.

On the right-hand side of Eq. (3.6), the $\tilde{x}$-dependence is hidden in the variable Y in the following way

$$Y = \ln\left(\frac{x_0}{\tilde{x}}\right), \quad (3.8)$$

where x_0 corresponds to the initial value of the $N(\vec{r},\vec{b},Y)$ evolution [22].

As mentioned earlier, one of the main observable prediction of the colour dipole model is that of the structure functions. These can be directly compared

[4]Such as the GBW model [19].

to an experimental output, such as in [26], or used to derive other quantities, e.g. the DIS cross section or the reduced cross section.

The relations to obtain the structure functions are [22]

$$F_2(x,Q^2) = \frac{Q^2}{4\pi^2\alpha_{em}}\left(\sigma_T^{\gamma^* p}(x,Q^2) + \sigma_L^{\gamma^* p}(x,Q^2)\right), \tag{3.9}$$

$$F_L(x,Q^2) = \frac{Q^2}{4\pi^2\alpha_{em}}\ \sigma_L^{\gamma^* p}(x,Q^2). \tag{3.10}$$

The F_L is the so-called longitudinal structure function. To a certain extent, it represents a correction to the Callan-Gross relation [12] and the assumption of the parton model, that the partons are fermions. The three structure functions are related by

$$F_2(x,Q^2) - 2xF_1(x,Q^2) = F_L(x,Q^2). \tag{3.11}$$

Another observable, often presented by experimental facilities [27, 28], is the reduced cross section [29]

$$\sigma_r(Q^2,x,y) = F_2(Q^2,x) - \frac{y^2}{1+(1-y)^2}F_L(Q^2,x). \tag{3.12}$$

The inelasticity y is connected to the virtuality Q, Bjorken x, and the centre-of-mass energy $\sqrt{s}$ by [29]

$$Q^2 = xys. \tag{3.13}$$

3.1 Unitarity constraints

The colour dipole model presents an alternative approach to the BFKL evolution equation by providing a way to study the unitarity and approach the saturation at low x [9].

An equivalent form of the BFKL equation for the dipole scattering amplitude prediction can be obtained in the form [30, 31]

$$\frac{\partial N(\vec{r},\vec{b},Y)}{\partial Y} = \int \mathrm{d}^2\vec{r_1} K_{BFKL}(r,r_1,r_2)\times \left[N(\vec{r_2},\vec{b}-\frac{\vec{r_1}}{2},Y) + N(\vec{r_1},\vec{b}-\frac{\vec{r_2}}{2},Y) - N(\vec{r},\vec{b},Y)\right], \tag{3.14}$$

where $\vec{r}$ denotes the size of a respective dipole, $\vec{b}$ is the collision form factor corresponding to Fig. 3.1, and the kernel is

$$K_{\mathrm{BFKL}}(r,r_1,r_2) = \frac{\alpha_s N_C}{2\pi^2}\frac{r^2}{r_1^2 r_2^2}. \tag{3.15}$$

Within the dipole model, the particular terms in Eq. (3.14) have a direct phenomenological interpretation as an annihilation of the size-$\vec{r}$ parent dipole (the negative one) and a simultaneous creation of daughter dipoles of sizes $\vec{r_1}$ and $\vec{r_2}$ (two positive ones).

Clearly, no mechanism of dipole recombination is present in the BFKL evolution, which is also the main reason for the uncontrolled gluon distribution low-x divergence, and subsequent unitarity violation.

Although the BFKL suffices to describe the currently available experimental data, saturation is a desirable mechanism to be included in the evolution.

Chapter 4

Saturation implementation

A non-linear term needs to be included in the evolution equation in order to introduce a recombination process and eventually a saturation of the gluon distribution function. Such a term is presented by the Balitsky-Kovchegov (BK) equation [32–36], which can be obtained from an effective theory of the Colour Glass Condensate.

4.1 The Colour Glass Condensate model

To describe the high-energy limit of QCD, the idea of the Colour Glass Condensate (CGC) is utilised [9, 37–40]. The CGC itself is a highly coherent ensemble of gluon states with extremely high energy density. In a high energy hadronic scattering, the CGC describes the pre-collision hadronic state. After the collision it evolves into the so-called Glasma, from which the quark gluon plasma and eventually a gas of ordinary hadrons emerge.

The word *colour* in the model name reflects the fact that the gluons carry the colour charge. The term *glass* refers to an analogy with an actual glass in the sense of exhibiting a solid-like behaviour on short time scales and a liquid-like behaviour on longer ones. Finally, the *condensate* corresponds to the high density of massless gluons within the system [37].

The idea behind the CGC as an effective field theory is to describe the high-energy QCD in the light cone formalism [41] as a many-body theory with a large number of partons. These are weakly coupled, but due to their large number, the description is non-perturbative.

There are assumed to be two kinds of partons based on their energy. The low-x "wee" partons are subject to evolution while the "valence" partons, carrying a high fractional momentum are treated as static[1] sources of colour charge. Due to their large momentum, they are assumed to be recoilless, unaffected by absorbing or emitting soft quanta [37].

[1]The wee-parton life time is much shorter than that of the valence ones.

The x-evolution of the CGC system is described by an infinite set of coupled Jalilian-Marian-Iancu-McLerran-Weigert-Leonidov-Kovner (JIMWLK) equations [17, 38, 40, 42, 43]. Unfortunately, due to its extreme complexity, no analytical solution is known.

However, there is a way to simplify the JIMWLK equations and obtain a single, so-called Balitsky-Kovchegov equation describing the colour dipole scattering amplitude.

In the limit of large N_C (number of QCD colours) [33, 44], the following approximation can be made: the gluon emission from the original dipole can be treated as equivalent to an emission of a coloured $\mathrm{q\bar{q}}$ pair as depicted in Fig. 4.1 [30]. Furthermore, the large-N_C limit allows one to replace a multiple gluon emission by a cascade of daughter dipoles.

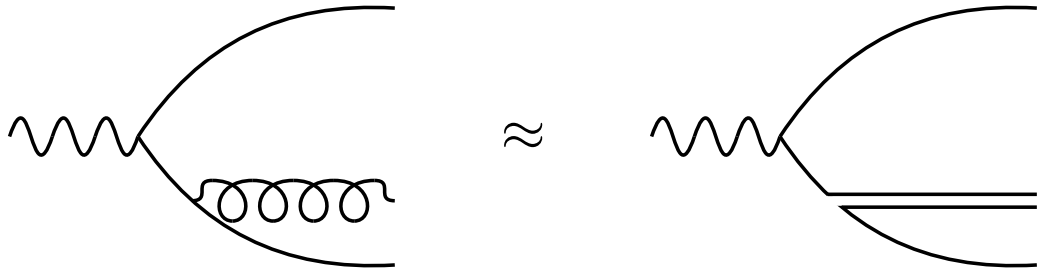

Fig. 4.1: The equivalence of the gluon emission and daughter dipole emergence in the large N_C limit.

4.2 The Balitsky-Kovchegov equation

The resulting Balitsky-Kovchegov equation describing the dipole evolution reads [32–36]

$$\frac{\partial N(\vec{r},\vec{b},Y)}{\partial Y} = \int \mathrm{d}\vec{r_1} K(r,r_1,r_2)\Big[N(\vec{r_1},\vec{b_1},Y) + N(\vec{r_2},\vec{b_2},Y) - N(\vec{r},\vec{b},Y) - N(\vec{r_1},\vec{b_1},Y)N(\vec{r_2},\vec{b_2},Y)\Big]. \tag{4.1}$$

As described earlier in this chapter, $N(\vec{r},\vec{b},Y)$ represents the scattering amplitude between a proton and a colour dipole of size $\vec{r}$ and impact parameter $\vec{b}$. The evolution equation describes the creation of two new dipoles $N(\vec{r_1},\vec{b_1},Y)$ and $N(\vec{r_2},\vec{b_2},Y)$ while simultaneously annihilating the original one. The geometric layout of the daughter dipole sizes and impact parameters is depicted in Fig. 4.2.

Unlike the BFKL evolution Eq. (3.14), the BK equation contains a negative non-linear term $N(\vec{r_1},\vec{b_1},Y)N(\vec{r_2},\vec{b_2},Y)$. It corresponds to the recombination

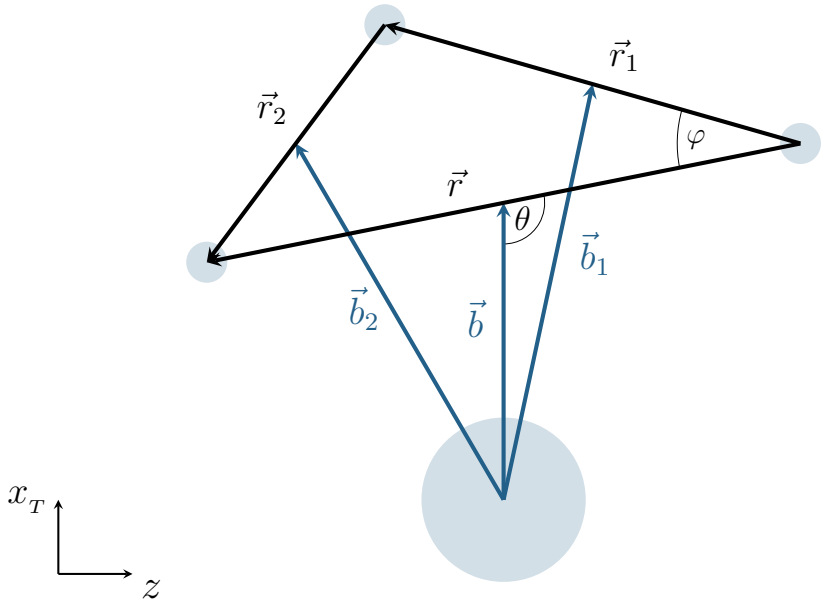

Fig. 4.2: The proton–dipole interaction geometry in the z, x_T plane (rotational symmetry of the problem is assumed with respect to the z-axis). The large blue sphere represents the proton, the small spheres depict the dipole and an emergent gluon in correspondence to Fig. 4.1. The vector $\vec{b}$ denotes the original dipole impact parameter and $\vec{b_j}$ is then the impact parameter of the j-th daughter dipole.

of two dipoles and at large gluon densities implements the aforementioned saturation mechanism.

4.2.1 The kernel

The function $K(r, r_1, r_2)$ is the kernel of the integro-differential equation, which in the case of the BK equation corresponds to the probability of gluon emission.

A simple version of a kernel has already been presented for the BFKL evolution equation in Eq. (3.14).

The running coupling kernel

Going further into the perturbative expansion and taking into account the running of the strong coupling, the so-called running coupling (rc) kernel is

obtained [26, 35]

$$K_{\mathrm{rc}}(r, r_1, r_2) = \frac{\alpha_s(r^2) N_C}{2\pi^2} \left[\frac{r^2}{r_1^2 r_2^2} + \frac{1}{r_1^2} \left(\frac{\alpha_s(r_1^2)}{\alpha_s(r_2^2)} - 1 \right) + \frac{1}{r_2^2} \left(\frac{\alpha_s(r_2^2)}{\alpha_s(r_1^2)} - 1 \right) \right]. \tag{4.2}$$

Here N_C is the number of colours and the r^2 dependence of the strong coupling is

$$\alpha_s(r^2) = \frac{4\pi}{\beta_{0,n_f} \ln\left(\frac{4C^2}{r^2 \Lambda_{n_f}^2} \right)}, \tag{4.3}$$

where C is a parameter to be determined by a fit to data and Λ_{n_f} is a scale parameter dependent on the number of active flavours.

The possible flavour of the dipole, emergent from the virtual photon, depends on the energy scale or equivalently the r-scale, because

$$\mu^2 = \frac{4C^2}{r^2}. \tag{4.4}$$

Therefore, reaching lower r^2 (or larger scales), heavier flavour pairs (c and b) can be produced and the number of active flavours n_f rises. These pairs then interact with the proton, which needs to be reflected in the running of the strong coupling. From Eq. (4.4), the values of r can be calculated, at which the n_f changes, based on the quark mass m_f by

$$r_{n_f} = \sqrt{\frac{4C^2}{m_f^2}}. \tag{4.5}$$

This way, the α_s range is split into regimes where 3, 4, and all 5 quark flavours are active[2] [22] as shown in Fig. 4.3.

The leading order coefficient of the QCD beta-series β_{0,n_f} reads

$$\beta_{0,n_f} = \frac{1}{3}(11 N_C - 2 n_f) \tag{4.6}$$

and can be simply calculated. To obtain the values of Λ_{n_f}, a matching condition must be placed on the α_s in the transition values, resulting in

$$\alpha_{s,n_f-1}(r_{n_f}) = \alpha_{s,n_f-1}(r_{n_f}) \quad \Rightarrow \quad \Lambda_{n_f-1} = m_f^{1-\frac{\beta_{0,n_f}}{\beta_{0,n_f-1}}} \Lambda_{n_f}^{\frac{\beta_{0,n_f}}{\beta_{0,n_f-1}}}. \tag{4.7}$$

[2]There is no splitting for $n_f < 3$, because the masses of the three light quarks are taken to be identical. Furthermore, for its enormous mass, the top quark is neglected within these calculations.

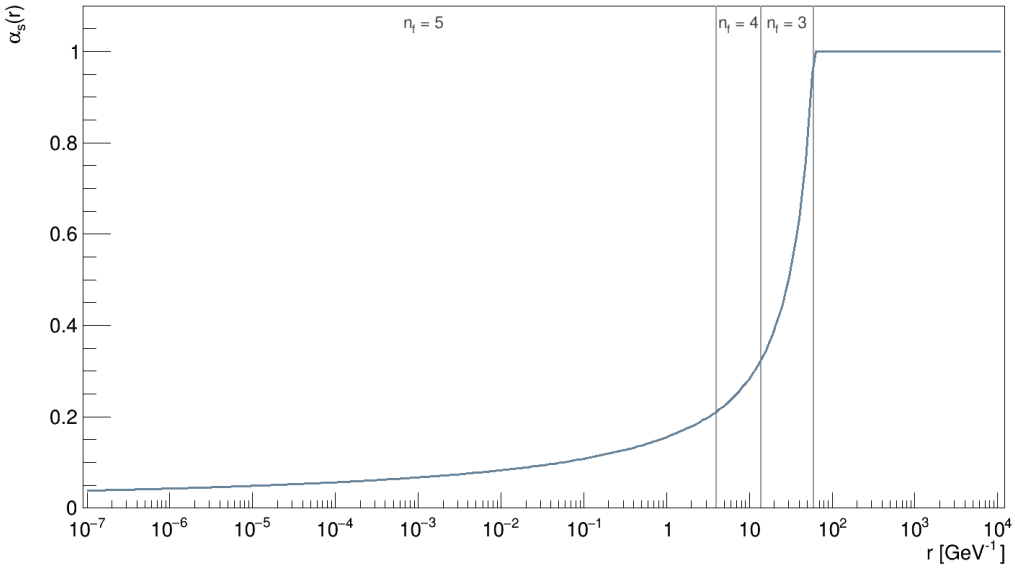

Fig. 4.3: The running of the strong coupling α_s saturated at $\alpha_{s_{max}} = 1$. The vertical lines denote the splitting of the range to sectors with the corresponding number of active flavours.

Having this recursive relation, the last thing to add is a starting point. A good choice is the experimentally measured value of $\alpha_s(M_Z^2)$ at the scale of the Z boson mass. From Eq. (4.3), the starting point is then

$$\Lambda_5 = \sqrt{\frac{4C^2}{r_Z^2} \exp\left[-\frac{\alpha_{s,5}\beta_{0,5}}{4\pi}\right]} = M_Z e^{-\frac{\alpha_{s,5}\beta_{0,5}}{2\pi}}. \tag{4.8}$$

Following [22, 45], the growth of α_s is restricted to some value $\alpha_{s_{max}}$ as shown in Fig. 4.3 with $\alpha_{s_{max}} = 1$. For a fixed n_f scheme, $\beta_{0,n_f} = \beta_0$ and $\Lambda_{n_f} = \Lambda_{QCD}$.

The collinearly improved kernel

Using the running coupling kernel, the BK equation can be numerically solved. However, in the case of the 2-dimensional BK equation[3], the results exhibit too fast a growth at large impact parameters, so-called Coulomb tails [45]. A new so-called collinearly improved (ci) kernel was presented in Ref. [45–47]

$$K_{\text{ci}} = \frac{\bar{\alpha}_s}{2\pi} \frac{r^2}{r_1^2 r_2^2} \left[\frac{r^2}{\min\{r_1^2, r_2^2\}}\right]^{\pm\bar{\alpha}_s A_1} \frac{J_1(2\rho\sqrt{\bar{\alpha}_s})}{\rho\sqrt{\bar{\alpha}_s}}. \tag{4.9}$$

[3]In the 2-D BK equation the dipole scattering amplitude is assumed to only depend (besides the rapidity Y) on the norms of the vectors $\vec{r}$ and $\vec{b}$.

Here J_1 is the Bessel function of the first kind, the parameter $A_1 = \frac{11}{12}$, and the sign of the power is positive when $r^2 < \min\{r_1^2, r_2^2\}$. The variable ρ is defined by

$$\rho = \sqrt{\left|\ln\left(\frac{r_1^2}{r^2}\right)\ln\left(\frac{r_2^2}{r^2}\right)\right|}. \tag{4.10}$$

The modified strong coupling $\bar{\alpha}_s$ is

$$\bar{\alpha}_s = \frac{\alpha_s(\min\{r^2, r_1^2, r_2^2\})N_C}{\pi}. \tag{4.11}$$

4.2.2 Initial condition

Being an integro-differential equation, the BK equation needs an initial condition to solve the differential component. Therefore, the scattering amplitude at rapidity $Y = 0$ needs to be specified.

Impact-parameter-independent initial conditions

For the $\vec{b}$ independent solution, two initial conditions are presented. The first one is inspired by the phenomenological model of Golec-Biernat Wüsthoff (GBW) [9, 19] and reads[22]

$$N_{\mathrm{GBW}}(\vec{r}, Y = 0) = 1 - \exp\left[-\frac{(r^2 Q_{s0}^2)^\gamma}{4}\right], \tag{4.12}$$

where both the parameters γ and Q_{s0} (the proton saturation scale) are to be determined by experimental data.

Another initial condition figures in the McLerran-Venugopalan model [22, 48]

$$N_{\mathrm{MV}}(\vec{r}, Y = 0) = 1 - \exp\left[-\frac{(r^2 Q_{s0}^2)^\gamma}{4}\ln\left(\frac{1}{r\Lambda_{QCD}} + e\right)\right], \tag{4.13}$$

where Λ_{QCD} denotes the QCD scale parameter.

To see the overall effects of the initial condition on the evolution, a modification of the Heaviside function was also used in the form

$$N_\theta(r, Y = 0) = \frac{1}{2}\theta(x - 3) = \begin{cases} 0 & r \leq 3 \\ 0.5 & r > 3 \end{cases}. \tag{4.14}$$

Impact-parameter-dependent initial condition

To obtain an initial condition for the $\vec{b}$-dependent BK equation, a combination of the GBW model for the $\vec{r}$ dependence and a Gaussian distribution for the impact parameter was used [45, 49]

$$N(\vec{r},\vec{b},Y=0)=1-\exp\left[-\frac{1}{2}\frac{r^2Q_s^2}{4}T(\vec{r},\vec{b})\right], \tag{4.15}$$

where

$$T(\vec{r},\vec{b})=\exp\left[-\frac{d_1^2(\vec{r},\vec{b})}{2B}\right]+\exp\left[-\frac{d_2^2(\vec{r},\vec{b})}{2B}\right]. \tag{4.16}$$

Both the saturation scale Q_s^2 and parameter B (which can be connected to the target profile [45]) are to be adjusted by fitting. The $\vec{b}$-dependence is hidden in the impact parameters of the quark and the antiquark as described in Appendix C.

Chapter 5

Solutions of the BK equation

As discussed earlier in this work, the BK equation implements the desirable mechanism of gluon saturation while being simpler to solve numerically than the infinite set of JIMWLK equations. Such a solution is presented for the 1-dimensional and 2-dimensional versions of the BK equation.

All methods and algorithms necessary for the numerical solution of the BK equation are implemented in C++.

5.1 Numerical methods

For the purpose of a clear numerical solution, the right-hand side of the BK equation Eq. (4.1) can be rewritten as[1]

$$\partial_Y N(\vec{r},\vec{b},Y) = I_1 - N(\vec{r},\vec{b},Y)I_0 - I_2, \tag{5.1}$$

where

$$I_0 = \int \mathtt{d}\vec{r_1} K(r,r_1,r_2) \equiv \int \mathcal{D}K, \tag{5.2}$$

$$I_1 = \int \mathcal{D}K \left[N(\vec{r_1},\vec{b_1},Y) + N(\vec{r_2},\vec{b_2},Y)\right], \tag{5.3}$$

$$I_2 = \int \mathcal{D}K N(\vec{r_1},\vec{b_1},Y)N(\vec{r_2},\vec{b_2},Y). \tag{5.4}$$

The integration measure $\mathcal{D}K$ was introduced for a clearer orientation in this and the following equations.

Once the integrals I_j are calculated, a simple differential equation is left to be solved.

[1]The operator ∂_Y denotes the partial derivative with respect to Y.

5.1.1 The differential equation solution

Containing no explicit rapidity dependence, the differential equation Eq. (5.1) can be solved using the Runge-Kutta method. Its form and description can be found in [50–52], however, it is fairly straightforward to derive at least the first order.

A function $f(\xi)$, analytical at a point a can be expanded into a Taylor series as

$$f(\xi) = f(a) + (\xi - a)\frac{\partial f}{\partial \xi}(a) + \mathcal{O}((\xi - a)^2). \tag{5.5}$$

To highlight the infinitesimal shift, let us denote $\xi - a \equiv h$, where $h \to 0$. Furthermore, let us change the function variable to $x = \xi - h$ to get the explicit form of the first-order Runge-Kutta method

$$\begin{aligned} f(x+h) &= f(x) + h\frac{\partial f}{\partial(x+h)}(x) + \mathcal{O}(h^2) \\ &= f(x) + h\partial_x f(x) + \mathcal{O}(h^2). \end{aligned} \tag{5.6}$$

This already can be applied to evolve the scattering amplitude $N(Y, \vec{r}, \vec{b})$ numerically; a step in rapidity $Y_0 \to Y_0 + h$ can be done, as the $\partial_Y N$ is defined by the r.h.s. of the BK equation Eq. (4.1)

$$N(Y+h, \vec{r}, \vec{b}) = N(Y, \vec{r}, \vec{b}) + h\Big(I_0 - N(\vec{r}, \vec{b}, Y)I_1 - I_2)\Big) + \mathcal{O}(h^2). \tag{5.7}$$

However, to improve the calculation precision, a higher (fourth) order Runge-Kutta method is utilised [50]

$$N(Y+h, \vec{r}, \vec{b}) = N(Y+h, \vec{r}, \vec{b}) + \frac{1}{6}k_1 + \frac{1}{3}k_2 + \frac{1}{3}k_3 + \frac{1}{6}k_4 + \mathcal{O}(h^5), \tag{5.8}$$

where

$$k_1 = h\bigg(I_1 - N(\vec{r}, \vec{b}, Y)I_0 - I_2\bigg), \tag{5.9}$$

$$k_2 = k_1 + h\bigg(\frac{k_1}{2}\left(I_0 - I_1\right) + \frac{k_1^2}{4}I_0\bigg), \tag{5.10}$$

$$k_3 = k_1 + h\bigg(\frac{k_2}{2}\left(I_0 - I_1\right) + \frac{k_2^2}{4}I_0\bigg), \tag{5.11}$$

$$k_4 = k_1 + h\bigg(k_3\left(I_0 - I_1\right) + k_3^2 I_0\bigg), \tag{5.12}$$

as shown in more detail in Appendix A.

As described in its definition Eq. (3.8), rapidity is connected to Bjorken x on which the structure functions depend. Therefore, the rapidity range must be chosen with respect to the desired Bjorken x range in which predictions of observables are supposed to be given. Following [22], the value $x_0 = 0.01$ is chosen for the (1-D) evolution starting point, fixing the maximal Bjorken x to approximately 0.01 at $Y = 0$. To follow the interest in the low-x region (orders of approximately 10^{-6} to 10^{-2}), where the BK equation is supposed to hold, the evolution should go to approximately $Y = 3$ to fit the currently available data. To give predictions for future experiment, the rapidity is chosen to range up to $Y = 10$. The step length was chosen to be $h = 0.01$ [45].

5.1.2 Numerical integration

From the geometric layout depicted in Fig. 4.2, it is clear that the vector $\vec{r_1}$ can be expressed in terms of its size r_1 and the angle φ. Therefore, the integrals Eq. (5.4) can be rewritten

$$I_0 = \int_0^{2\pi} \mathtt{d}\varphi \int \mathtt{d}r_1 r_1 K(r, r_1, r_2) = 2\pi \int \mathtt{d}r_1 r_1 K(r, r_1, r_2), \tag{5.13}$$

$$I_1 = \int_0^{2\pi} \mathtt{d}\varphi \int \mathtt{d}r_1 r_1 K(r, r_1, r_2) \left[N(\vec{r_1}, \vec{b_1}, Y) + N(\vec{r_2}, \vec{b_2}, Y) \right], \tag{5.14}$$

$$I_2 = \int_0^{2\pi} \mathtt{d}\varphi \int \mathtt{d}r_1 r_1 K(r, r_1, r_2) N(\vec{r_1}, \vec{b_1}, Y) N(\vec{r_2}, \vec{b_2}, Y), \tag{5.15}$$

with $\vec{r_1}(r_1, \varphi)$ and $\vec{r_2}(r_1, r, \varphi)$.

To calculate a step in rapidity evolution, these integrals need to be evaluated per each point of the N domain[2]. To do so, the extended Simpson's rule is utilised [50, 51]. It sums the values of a function $f(x)$ in $n + 1$ points as

$$\int_{x_0}^{x_n} f(x)\mathtt{d}x = \frac{x_n - x_0}{3n} \left[f(x_0) + 2 \sum_{j=1}^{\frac{n}{2}-1} f(x_{2j}) + 4 \sum_{j=1}^{\frac{n}{2}} f(x_{2j-1}) + f(x_n) \right] + \mathcal{O}\left(\frac{1}{n^4}\right), \tag{5.16}$$

with even number n of equidistant steps.

[2] E.g. for a 2-dimensional BK equation with 100 points in r, 100 points in b and 20 points in φ, $100 \cdot 100 \cdot 20 \cdot 3$ integrals need to be evaluated in one rapidity step.

A modification of the Simpson's method was used to evaluate the integrals of logarithmically sampled functions[3]

$$\int_{x_0}^{x_n} f(x)\mathtt{d}x = \ln(10)\frac{x_n - x_0}{3n}\Big[x_0 f(x_0) + 2\sum_{j=1}^{\frac{n}{2}-1} x_{2j} f(x_{2j}) + 4\sum_{j=1}^{\frac{n}{2}} x_{2j-1} f(x_{2j-1}) + x_n f(x_n)\Big] + \mathcal{O}\left(\frac{1}{n^4}\right), \tag{5.17}$$

as further described in Appendix B.

5.2 The 1-dimensional solution

As discussed in Chapter 3, as an approximative approach, the impact parameter dependence can be integrated out of the BK equation into a fit parameter σ_0, see Eq. (3.7). In this 1-dimensional case, the only variable (except the rapidity Y in which the evolution takes place) is the dipole size $r \equiv |\vec{r}|$. Furthermore, utilising that

$$\vec{r_2} = \vec{r} - \vec{r_1} \quad \rightarrow \quad r_2 = \sqrt{r^2 + r_1^2 - 2rr_1\cos\varphi}, \tag{5.18}$$

the 1-dimensional BK equation reads

$$\partial_Y N(r,Y) = \int_0^{2\pi} \mathtt{d}\varphi \int \mathtt{d}r_1 r_1 K(r,r_1,\varphi)\Big[N(r_1,Y) + N(r_2(r,r_1,\varphi),Y) - N(r,Y) - N(r_1,Y)N(r_2(r,r_1,\varphi),Y)\Big]. \tag{5.19}$$

As mentioned in the previous section, the rapidity grid is chosen from $Y_0 = 0$ to $Y_{n_Y} = 10$ with step $h_Y = 0.01$, so that

$$Y_j = Y_0 + jh_Y, \quad j \in [0,100] \cap \mathbb{N}_0. \tag{5.20}$$

The r-grid ranges from $r_0 = 10^{-7}$ to $r_{n_r} = 10^2$. The r scale is logarithmic with a constant number of steps per order of magnitude[4] $n_{r,log} = 25$ which must be equidistant, so that an effective logarithmic Simpson's method can be used to calculate the r_1 integrals. Furthermore, the total number of steps n_r must be even, therefore, the j-th value of r in the grid is

$$r_j = r_0 10^{\,jh_{r,log}}, \quad j \in [0,n_r] \cap \mathbb{N}_0, \tag{5.21}$$

[3]With equidistant steps in the logarithmic scale $h = \log_{10} x_j - \log_{10} x_{j-1}$.

[4]In this case equal to the inverse logarithmic step length $h_{r,log} = \frac{1}{n_{r,log}}$.

and the total number of steps is

$$n_r = n_{r,log}\left(\log_{10}(r_0) - \log_{10}(r_{n_r})\right) + \alpha. \tag{5.22}$$

In this case, $n_r = 226$, as the parameter $\alpha \in \{0, 1\}$ ensures that n_r is even and the Simpson's method can be used. The r_1 grid is chosen to be the same, so that evaluating $N(r_1, Y)$ is effective when calculating the I_0, I_1, and I_2 integrals.

To calculate the integrals I_1 and I_2, the values of the dipole scattering amplitude $N(r_2, Y)$ are needed. As seen from Eq. (5.18), the values of r_2 do not necessarily coincide with the r-grid and $N(r_2, Y)$ needs to be interpolated. A simple linear Lagrange interpolation [50] is used to approximate the values of $N(r_2, Y)$ in r_2 between r_{min} and r_{max}.

$$N(r_2, Y) = N(r_a, Y)\frac{r_2 - r_b}{r_a - r_b} + N(r_b, Y)\frac{r_2 - r_a}{r_b - r_a}, \tag{5.23}$$

where a and b are the grid indices, namely, $a \in [0, n_r - 1] \cap \mathbb{N}_0$ so that $N(r_{2,a}, Y)$ indexes the largest value of N on the grid smaller than $N(r_2, Y)$ and $b = a + 1$.

For values of r_2 outside the grid, no particular extrapolation is utilised and simply the boundary value at the last (or the first) point of the grid is used.

To integrate over φ from 0 to 2π, an equidistant grid of 20 steps was chosen.

Initial condition comparison

The 1-dimensional BK equation was solved with the running coupling kernel Eq. (4.2) in a scheme with fixed $n_f = 3$. The required parameters were chosen following [22, 26] and can be found in Tab. 5.1 and Tab. 5.2.

To see the effect of the initial condition on the evolution, three different initial conditions were used; the GBW Eq. (4.12), MV Eq. (4.13), and the modified Heaviside Eq. (4.14). Together with the kernel parameters, the parameters required in the initial conditions are summarised in Tab. 5.1 and Tab. 5.2.

The comparison of the resulting scattering amplitudes for different initial conditions are depicted in Fig. 5.1 at several stages of the evolution (various rapidity values).

The most significant feature of Fig. 5.1 is the relative unimportance of the initial condition shape. It can be seen from the comparison of the model-dependent initial conditions GBW (blue) and MV (red), both of which gain the same shape during the evolution. To get a clearer example, they can be compared to the unphysical modified Heaviside function (yellow), which was chosen such that not even its range coincides with that of the GBW or MV. Still, after ~ 200 steps (at rapidity $Y \sim 2$), the shape of the scattering amplitude is the same as for the physically motivated initial conditions.

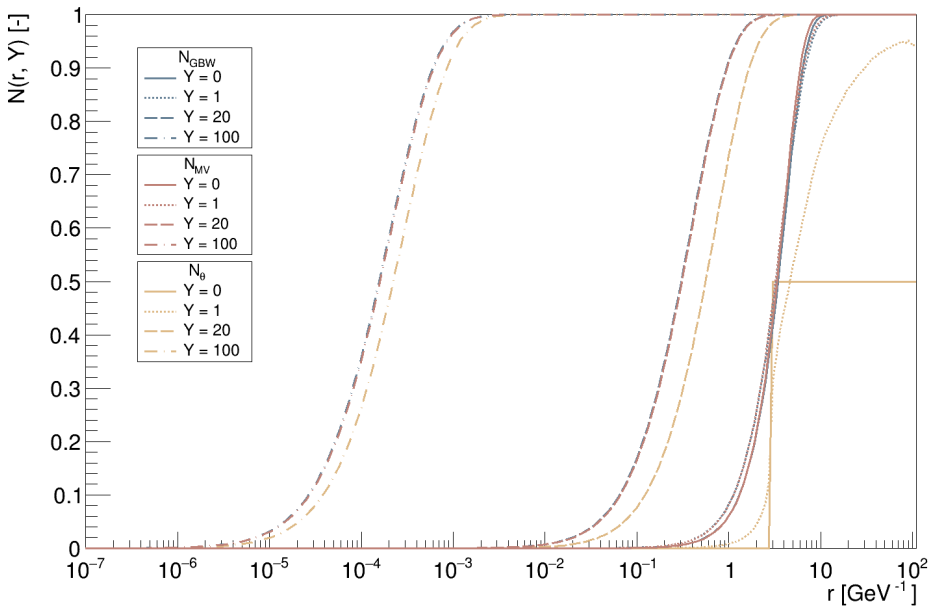

Fig. 5.1: A comparison of the scattering amplitudes as functions of the dipole size r at rapidities $Y = 0, 1, 20, 100$ as results of the BK equation with the running coupling kernel and various initial conditions (GBW - blue, MV - red, Heaviside - yellow).

An extensive comparison is shown in Fig. 5.2 and Fig. 5.3, where the full 2-dimensional dependence of $N(r, Y)$ is shown. While in the first figure, the BK equation forces the desired shape of the dipole scattering amplitude fairly quickly (note the small initial decrease at r between 1 and 10 GeV^{-1} followed by the monotonic behaviour), the latter figure captures a far more significant initial evolution.

C	Λ_{QCD} [GeV]	$\alpha_{s,max}$	Q_{s0} [GeV^2]	γ	$m_{u,d,s}$[MeV]	σ_0[mb]
2.52	0.241	0.7	0.165	1.135	140	32.895

Tab. 5.1: Numerical values of parameters for the 1-dimensional BK equation solution in the MV model [22].

C	Λ_{QCD} [GeV]	$\alpha_{s,max}$	Q_{s0} [GeV^2]	γ	$m_{u,d,s}$[MeV]	σ_0[mb]
2.46	0.241	0.7	0.241	0.971	140	32.357

Tab. 5.2: Numerical values of parameters for the 1-dimensional BK equation solution in the GBW model [22].

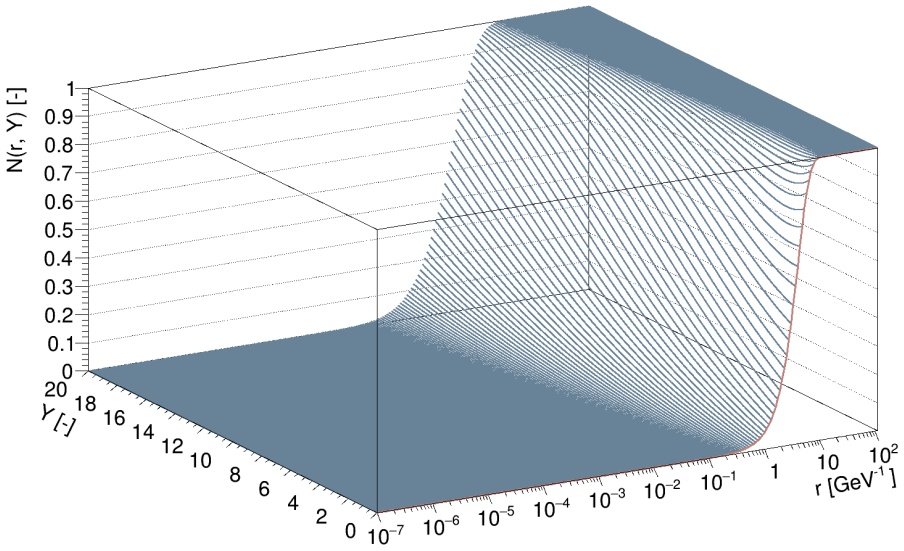

Fig. 5.2: The scattering amplitude as a function of rapidity Y and dipole size r from the solution of the BK equation with the running coupling kernel and the MV initial condition (highlighted in red).

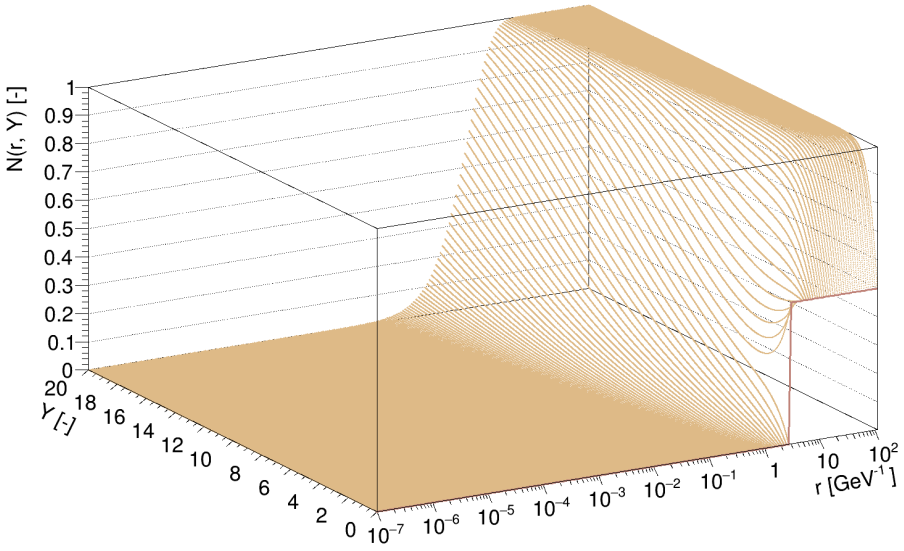

Fig. 5.3: The scattering amplitude as a function of rapidity Y and dipole size r from the solution of the BK equation with the running coupling kernel and the Heaviside initial condition (highlighted in red).

The non-linear term effect

As described in Chapter 4, the BK equation implements the effect of parton saturation with the non-linear term, which represents the gluon recombination. To point out the main difference between the BK equation Eq. (5.24) and the linear BFKL equation Eq. (5.25), their 1-dimensional form can be written

$$\partial_Y N(r,Y) = \int \mathcal{D}K \left[N(r_1,Y) + N(r_2,Y) - N(r,Y) + N(r_1,Y)N(r_2,Y) \right], \tag{5.24}$$

$$\partial_Y N(r,Y) = \int \mathcal{D}K \left[N(r_1,Y) + N(r_2,Y) - N(r,Y) \right]. \tag{5.25}$$

An illustrative solution of both evolutions with the same kernels and initial conditions was calculated for two values of the dipole size r. The resulting evolution is depicted in Fig. 5.4.

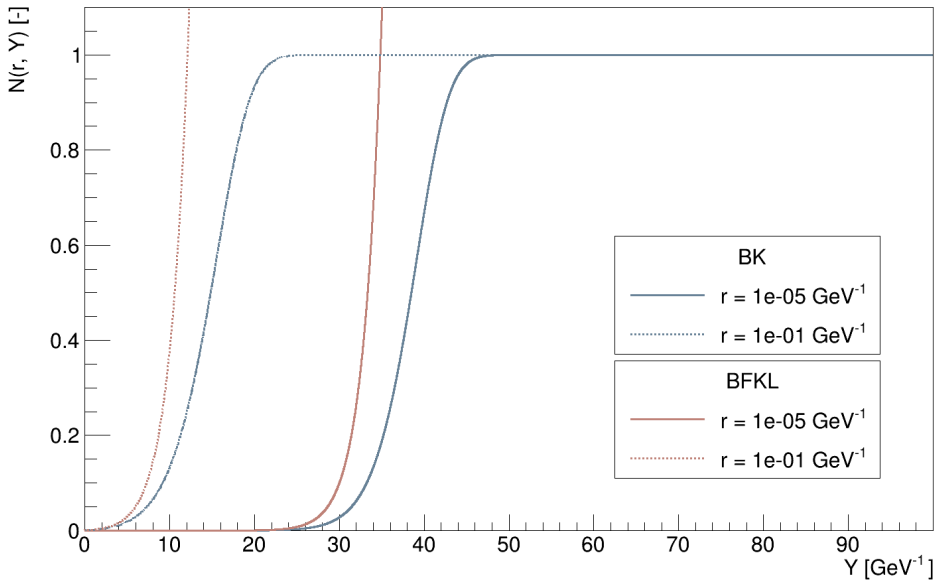

Fig. 5.4: The dipole scattering amplitude as a solution of the BK (blue) and the BFKL (red) evolution equations with the MV initial condition and the BFKL kernel for dipole sizes $r = 10^{-5}\text{GeV}^{-1}$ (full line) and $r = 2.51189\text{GeV}^{-1}$ (dashed line).

In both cases, the MV initial condition Eq. (4.13) was chosen with parameters from Tab. 5.1 and the simple BFKL kernel Eq. (3.15) was used with a fixed value of the strong coupling $\alpha_s = 0.19$, following [16].

The message of Fig. 5.4 is clear; the negative non-linear term of the BK equation becomes dominant at high rapidities (or equivalently in the region

of low Bjorken x, see Chapter 3) resulting in the saturation of the dipole scattering amplitudes. The linear BFKL evolution has no such mechanism and soars extremely quickly with increasing rapidity.

5.3 The 2-dimensional solution

Besides the dipole size, the state-of-the-art solution of the BK equation takes into account another variable; the norm of the impact parameter vector $b \equiv |\vec{b}|$. The 2-dimensional BK equation reads

$$\partial_Y N(r,b,Y) = \int \mathcal{D}K \Big[N(r_1,b_1,Y) + N(r_2,b_2,Y) - N(r,b,Y) - N(r_1,b_1,Y)N(r_2,b_2,Y) \Big]. \tag{5.26}$$

The maximum of the grid for the r domain is extended[5] from 10^2 to 10^4 for the 2-dimensional solution. The grid of the second dimension b was defined to be the same as of r.

Computationally, the main difference from the 1-dimensional case is the need to interpolate a function of two variables, namely, $N(r_2, b_2, Y)$. To do so, the bilinear interpolation [50] is used. In the case of the (logarithmically) equidistant grid, it utilises 4 grid points (r_a, r_b, b_a, b_b) which form a rectangle around the point of interest. The way in which the impact parameters b_1 and b_2 are calculated from the collision geometric layout is further described in Appendix C. The notation follows the linear Lagrange interpolation Eq. (5.23), so that $b = a + 1$ and both indices lie on the grid. The bilinear interpolation formula reads

$$N(r_2,b_2,y) = (1-t)(1-u)N(r_a,b_a,y) + t(1-u)N(r_b,b_a,y) \tag{5.27}$$

$$+tuN(r_b,b_b,y) + (1-t)uN(r_a,b_b,y), \tag{5.28}$$

where

$$t = \frac{r_2 - r_a}{r_b - r_a}, \tag{5.29}$$

$$u = \frac{b_2 - b_a}{b_b - b_a}. \tag{5.30}$$

Different generic multivariate interpolation methods have been tested using, e.g. the calculation of Vandermonde determinants. However, the code complexity increased rapidly, making the calculation extremely ineffective, whilst not improving its precision.

[5] In order to prepare the solution for the calculation of nuclear scattering processes reaching higher values of r and b.

Two examples of the scattering amplitudes $N(r, b, Y)$ as results of the 2-dimensional BK equation are shown in Fig. 5.5. The value of the angle between the impact parameter and the original dipole (see Fig. 4.2) was fixed to $\theta = \pi$. The left histogram depicts the b-dependent initial condition Eq. (4.15), whilst the right one captures the scattering amplitude evolved to rapidity $Y = 10$ using the collinearly improved kernel Eq. (4.9) in a variable n_f scheme up to $n_f = 5$. The running of the strong coupling $a_s(r)$ is fixed to $\alpha_{s_{max}} = 1$ and the parameters Λ_{n_f} are calculated recursively as described by Eq. (4.7), starting at $\alpha_s(M_Z^2) = 0.1189$ for $M_Z = 91.18\text{GeV}$ [15]. The quark masses and remaining necessary parameters are defined in Tab. 5.3, following [45]. The parameters were fitted for a situation where the initial condition does not depend on θ, which effectively corresponds to using $\theta = \frac{\pi}{2}$ in Eq. (4.15). The subsequent evolution was calculated for the value $\theta = \pi$. To have access to the correct fit parameters, and therefore be able to produce the predictions of observable quantities in this section, the same set-up has been used to calculate the *mixed* 2-dimensional BK equation solution. Solutions using the same value of θ for both the initial condition and the evolution, namely $\theta = \pi$ and $\theta = \frac{\pi}{2}$, are presented at the end of the section and will be a subject of studies following this thesis.

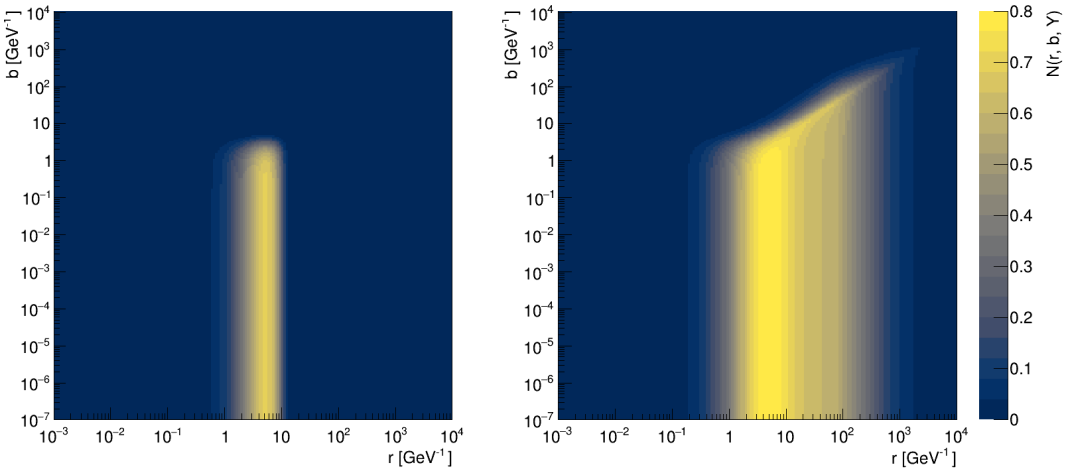

Fig. 5.5: An evolution of the b-dependent initial condition at $\theta = \frac{\pi}{2}$ (left) to the scattering amplitude at rapidity $Y = 10$ (right) with the mixed (using $\theta = \pi$) 2-dimensional BK equation. The evolution is driven by the collinearly kernel in a variable n_f scheme with parameters defined in Tab. 5.3.

The choice of the collinearly improved kernel follows from a problem connected to the running coupling kernel. When it is used to solve the the 2-dimensional BK equation, the so-called Coulomb tails [45] emerge as shown in Fig. 5.6. These contributions to the scattering amplitude at large values of the

C	Q_{s0} [GeV^2]	γ	B [GeV^{-2}]	$m_{u,d,s}$ [MeV]	m_c [GeV]	m_b [GeV]
9	0.496	1.135	3.2258	100	1.3	4.2

Tab. 5.3: Numerical values of parameters for the 2-dimensional BK equation solution [45].

impact parameter grow too fast and have to be curbed by introducing extra ad hoc terms within the kernel itself. An alternative to this approach is given by introducing the collinearly improved kernel, which controls the Coulomb tails intrinsically as further described in [45]. This phenomenon is clearly visible in the comparison between the BK equation solution with the running coupling (red) and the collinearly improved (blue) kernel in Fig. 5.6.

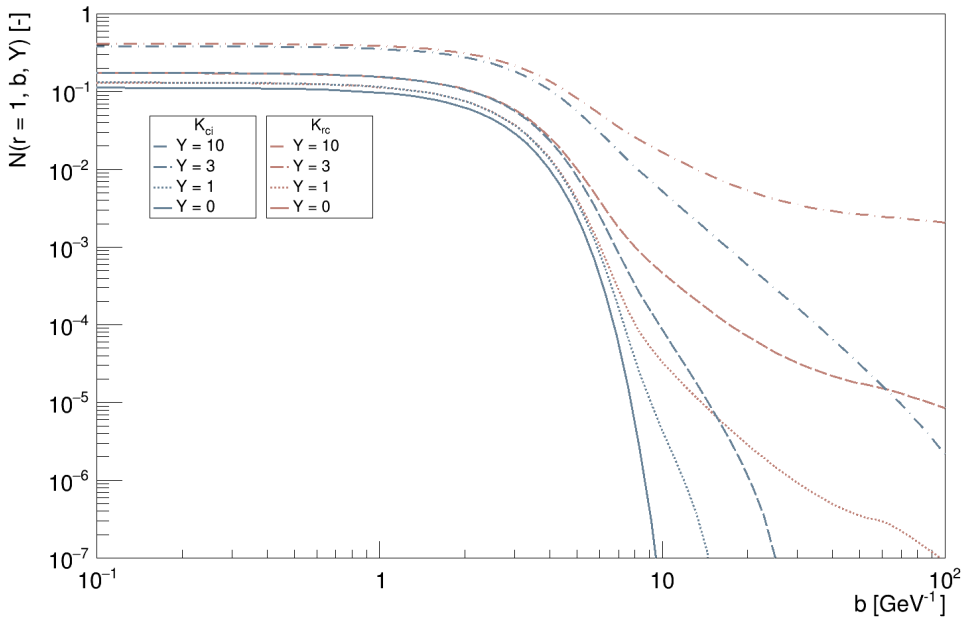

Fig. 5.6: A comparison of the mixed BK equation solutions with the running coupling kernel (red) and the collinearly improved kernel (blue) showing the curbing of the coulomb tails (large values of N at high b) by switching kernels. Same parameters have been used for both kernels.

To use the dipole amplitude for further calculations, the integral over $\vec{b}$ is performed to obtain the dipole cross section Eq. (3.6). In Fig. 5.7 a comparison of the integrated dipole amplitude for the running coupling (red) and the collinearly improved (blue) kernels is shown. Here, the Coulomb tails cause a rapid increase, which eventually leads to a disagreement of the predictions with the experimental data as shown in Chapter 6.

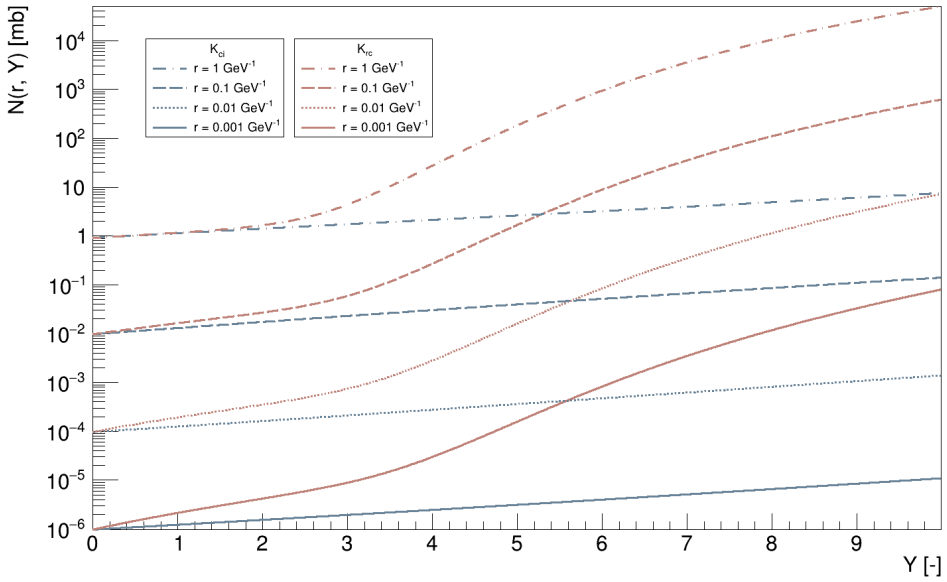

Fig. 5.7: The integrated dipole scattering amplitude evolving with rapidity Y for fixed values of the dipole size r. Solutions of mixed BK equation with two different kernels are shown to emphasise the effect of the Coulomb tails resulting from the running coupling kernel (red) compared to the solution with the collinearly improved kernel (blue).

For a qualitative comparison with the 1-dimensional solution, the full evolution of the integrated dipole amplitude from the 2-dimensional solution is shown in Fig. 5.8 in correspondence with Fig. 5.2 and Fig. 5.3.

The first thing to notice is the divergence towards high rapidities Y and dipole sizes r. However, this regime of large dipoles[6] is suppressed in further calculation of observable quantities.

The second important feature is that the initial condition does not seem to correspond well to the evolution equation. The original crest of the initial condition wave (red) is slowly replaced by a higher wave with a maximum at larger dipole sizes r. This behaviour suggests that a better initial condition could be constructed by tracing back the evolution from a point where the original physically motivated initial condition can be neglected to obtain a new initial condition that corresponds to the evolution as well as possible. Such attempts have been made in the 1-dimensional solution, however, the poor correspondence with experimental data suggests no special support of trying such a procedure in the 2-dimensional case.

[6]Compared to the proton charge radius $r_p \approx 0.17$ GeV^{-1} [15].

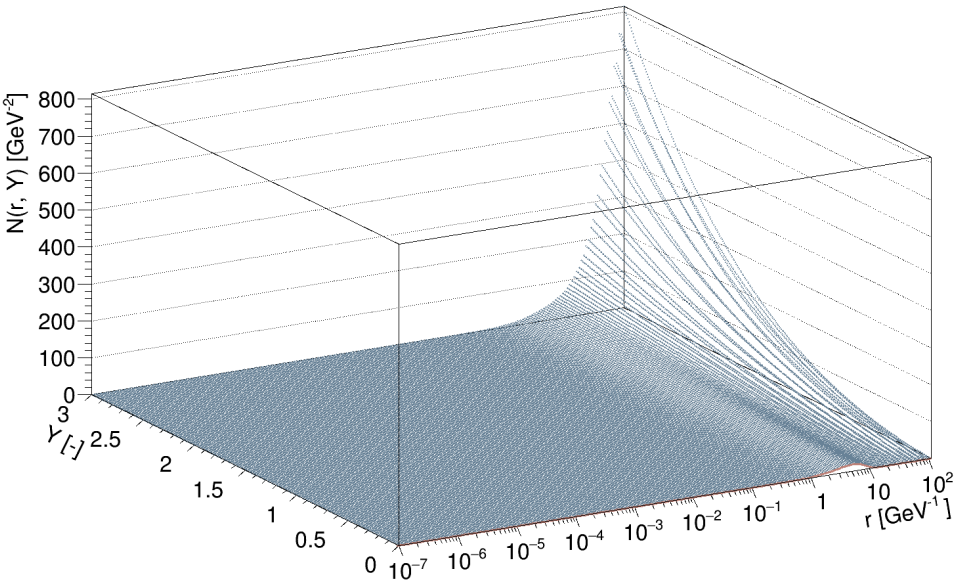

Fig. 5.8: A full evolution of the integrated dipole scattering amplitude from the integrated b-dependent initial condition at $\theta = \frac{\pi}{2}$ (red) as a solution of the mixed 2-D BK equation at $\theta = \pi$.

A possible reason for the mismatch between the initial condition and the evolution might be the different choice of the θ value ($\theta = \frac{\pi}{2}$ for the initial condition and $\theta = \pi$ for the evolution) as described earlier in this section. The 2-dimensional BK equation calculation was therefore conducted again for $\theta = \pi$ everywhere and the resulting integrated dipole scattering amplitude is shown in Fig. 5.9. Apparently, the evolution trend follows the original solution (with various θ values) and the aforementioned mismatch is not caused by the different θ in the initial condition.

To provide a glimpse of future calculations leading to the 3-dimensional BK equation solutions, a 2-dimensional solution for $\theta = \frac{\pi}{2}$ is presented in Fig. 5.10. Here the correspondence between the initial condition and the evolution shape is apparent, opening the question whether a different choice of the initial condition should be made for the future 3-D BK equation solutions.

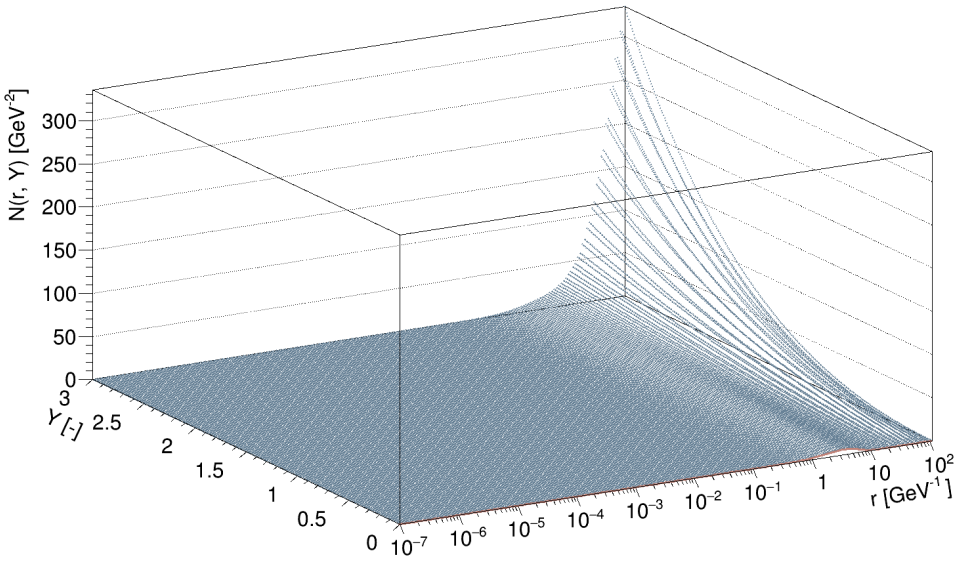

Fig. 5.9: A full evolution of the integrated dipole scattering amplitude from the integrated b-dependent initial condition at $\theta = \pi$ (red) as a solution of the mixed 2-D BK equation at $\theta = \pi$.

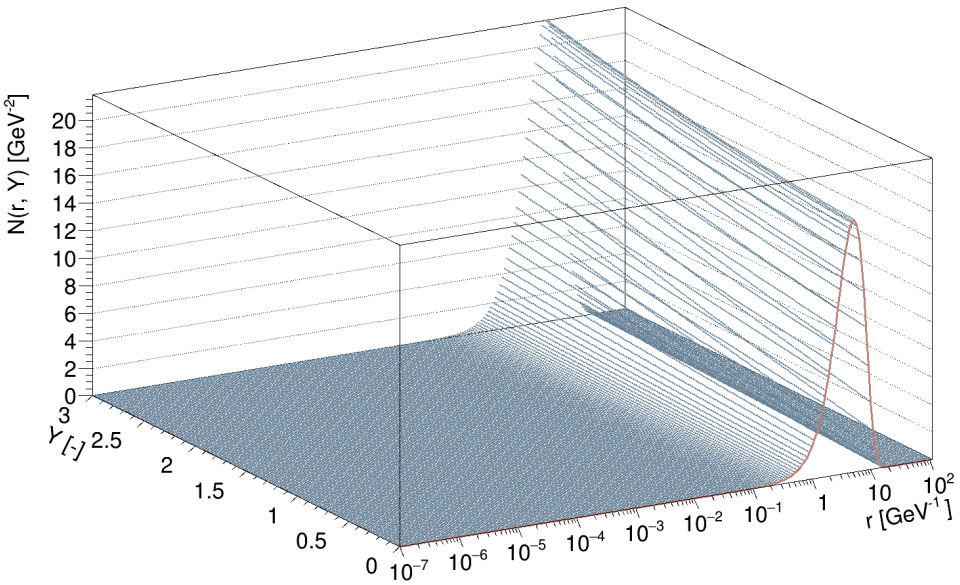

Fig. 5.10: A full evolution of the integrated dipole scattering amplitude from the integrated b-dependent initial condition at $\theta = \frac{\pi}{2}$ (red) as a solution of the 2-D BK equation at $\theta = \frac{\pi}{2}$.

Chapter 6

Prediction of observable quantities

Besides solving the BK equation, one of the main goals of this thesis is to also provide predictions of the real world behaviour by calculating observable quantities. To be able to compare the predictions with experimental data, two currently available observables were chosen; the structure functions, namely, the function $F_2(x, Q^2)$ and the reduced cross section $\sigma_r(x, Q^2)$. Both were a subject of measurement at the particle accelerator HERA, where protons were collided with electrons or positrons. The data used in this work are a combination of the results of the H1 and ZEUS collaborations [1] published in [27, 28].

At the time of the HERA operation, only a limited maximal collision energy was reachable[2] probing only a restricted region of low Bjorken x. In the presented analysis, the data from positron-proton collisions are used as they reach the lowest values of $x \sim 10^{-5}$. The lowest usable[3] values of x in the electron-proton data only reach $x \sim 10^{-3}$.

As new experimental facilities (especially electron-ion colliders) are to be constructed, it should be possible to probe the region of even lower Bjorken x, and further predictions of the theory described in this work can thus be put to test.

Several plots have been generated to show a comparison between the aforementioned data and the theoretically predicted observables, thus providing a proof of concept for the effective theory of the Colour Glass Condensate and its results in the form of the Balitsky-Kovchegov equation. Solutions of both 1-dimensional and 2-dimensional BK equations (described in the previous

[1] Both H1 and ZEUS were experiments at HERA.

[2] The maximal centre-of-mass energy of the HERA collisions analysed within this work is $\sqrt{s} = 319$ GeV.

[3] Usable meaning, that there are at least 4 low-x data points at a fixed virtuality.

chapter) have been used to obtain the proton structure function $F_2(x, Q^2)$ and the reduced cross section $\sigma_r(x, Q^2)$ as described in detail in Chapter 3.

6.1 The structure function F_2

Firstly, the two solutions of the 1-dimensional BK equation with the physically motivated initial conditions (GBW and MV) presented in Chapter 5 were used to calculate the F_2 structure function. All necessary parameters are given in Tab. 5.1 and Tab. 5.2. Only three active quarks with mass $m_{u,d,s} = 100$ MeV are taken into account so that the experimental data at large values of $x \sim 10^{-2}$ can also be described[4].

The results are shown in Fig. 6.1 for various values of virtuality Q^2 in comparison with experimental data from the positron–proton collisions at $\sqrt{s} = 319$ GeV [27].

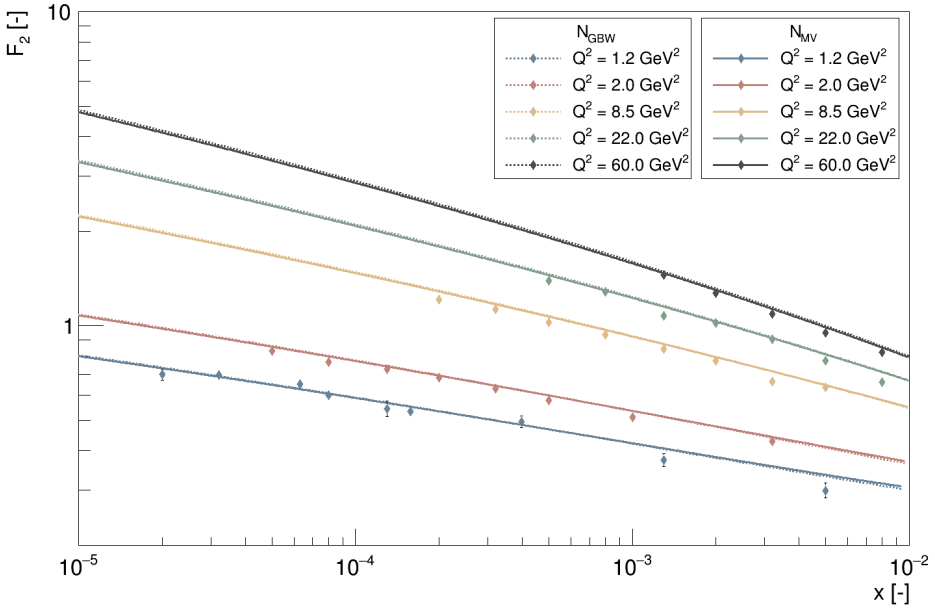

Fig. 6.1: The prediction of the structure function F_2 based on the 1-dimensional BK equation solution for various fixed virtuality values in comparison with experimental data from e^+p collisions at HERA [27].

[4]Taking even the lightest (of the heavy) charm quark with $m_c = 1.3$ GeV decreases the maximal x domain by almost an order of magnitude. It can be seen in Fig. 6.2 where four active flavours are taken into account and the predictions can only be calculated up to $x \sim 10^{-3}$ at virtuality $Q^2 = 1.2$ GeV^2.

No major effect of choosing a particular one of the two discussed initial conditions is visible. The only slight deviation between the predicted structure functions can be seen at high x at the lowest virtuality $Q^2 = 1.2$ GeV^2, where the dotted line of the GBW model goes somewhat under the full MV line.

In general, the 1-dimensional solution exhibits superior data agreement as compared to the 2-dimensional solution. The reason may be attributed to the presence of an additional free fit parameter in the form of the σ_0 from Eq. (3.7). It comes from the fact that the impact-parameter dependence of the dipole scattering amplitude is modelled by a theta function $\theta(\vec{b}_0 - \vec{b})$ in the 1-dimensional solution. The choice of the norm of the vector $\vec{b}_0$ is then left to be adjusted by fitting the resulting observables to the experimental data.

The 2-dimensional BK equation solution results in the F_2 prediction shown in Fig. 6.2 in comparison with the same experimental data as in the 1-dimensional case. As described in Chapter 5, the mixed solution was used, meaning that the initial condition Eq. (4.15) was evaluated at $\theta = \frac{\pi}{2}$ but during the evolution the value $\theta = \pi$ was used.

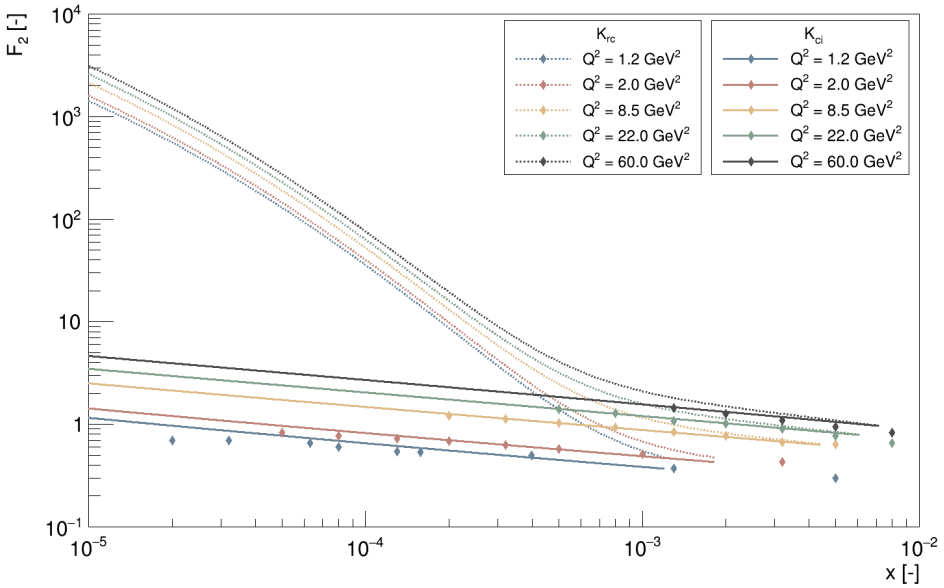

Fig. 6.2: The prediction of the structure function F_2 based on the 2-dimensional BK equation solution for various fixed virtuality values. Two kernels were used in the solution: the running coupling kernel (dotted line) and the collinearly improved kernel (full line). Comparison with experimental data from e^+p collisions at HERA [27].

Therefore, the parameters calculated in [45] could have been used as shown in Tab. 5.3. Four active flavours were used to calculate the structure functions,

resulting in the restricted domain of the predictions[5] in Fig. 6.2. Furthermore, unlike in the 1-dimensional case, the starting point of the evolution was set to be $x_0 = 0.008$.

The predictions of $F_2(x, Q^2)$ were calculated using solutions of the 2-dimensional BK equation driven by both the running coupling kernel and the collinearly improved kernel to show the ultimate reason for the necessity of introducing the latter. Clearly, the running coupling kernel driven evolution completely fails to describe the experimental data in the region of low x values, see Fig. 6.2. The collinearly improved kernel, on the other hand, provides a satisfying data agreement.

6.2 The reduced cross section σ_r

Having the structure functions calculated, the next step can be taken by presenting the predictions of the reduced cross section Eq. (3.12). This analysis is shown to provide a comparison with the latest[6] experimental data [28]. They again come from the positron–proton collisions, this time at $\sqrt{s} = 318$ GeV.

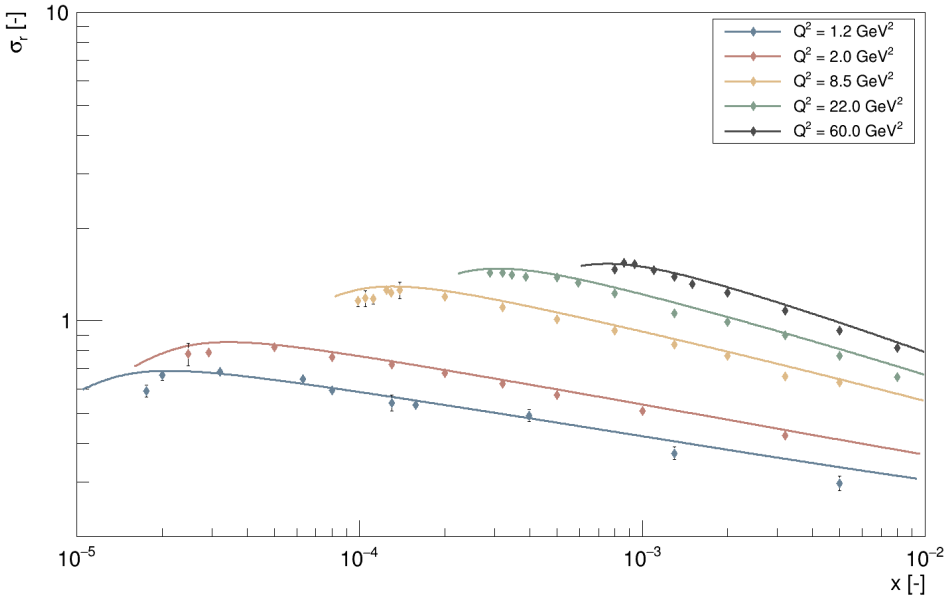

Fig. 6.3: The prediction of the reduced cross section σ_r based on the 1-dimensional BK equation solution for various virtuality values. Comparison with experimental data from e^+p collisions at $\sqrt{s} = 318$ GeV at HERA [28].

[5] Namely those at low virtuality Q^2.

[6] For the simple reason, that the latest HERA results do not directly show the F_2 measurements anymore.

For the 1-dimensional case, only the solution starting at the MV initial condition was used to get the predictions presented in Fig. 6.3. As the inelasticity y grows, the F_L structure function starts to contribute to the reduced cross section σ_r more significantly. At fixed virtuality Q^2, the increase in the inelasticity y corresponds to a decrease of the Bjorken x (see Eq. (3.13)), resulting in a visible dip in the measured data. This behaviour is followed by the shape of the calculated function satisfyingly.

Similarly to the previous case, the 1-dimensional BK equation solution provides a better data description as seen by comparison of Fig. 6.3 and Fig. 6.4. The results of the mixed 2-dimensional solution, for which the necessary parameters were calculated in [45], is depicted by the full line in Fig. 6.4.

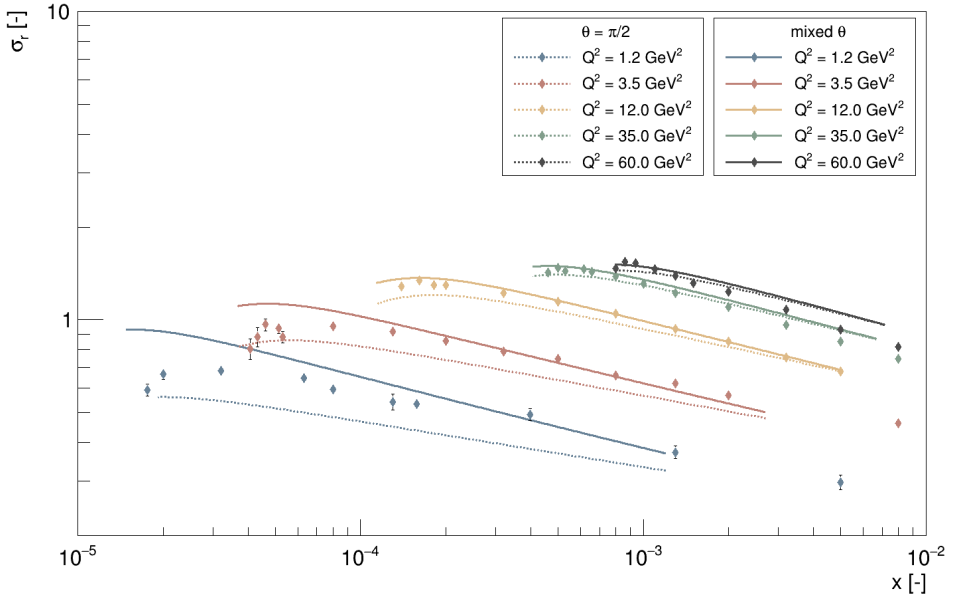

Fig. 6.4: The prediction of the reduced cross section σ_r based on the mixed 2-dimensional BK equation solution (full line) and solution with $\theta = \frac{\pi}{2}$ (dashed line) for various virtuality values. Comparison with experimental data from e^+p collisions at $\sqrt{s} = 318$ GeV at HERA [28].

Again, for a glimpse of the future 3-dimensional BK equation solution, the reduced cross section σ_r was also calculated for the $\theta = \frac{\pi}{2}$. It is depicted by the dashed line in Fig. 6.4 in comparison with the mixed solution. It cannot be said to describe the data better, after all, the incorrect fit parameters are used and it serves merely as an illustrative solution. Still, the deviations from the experimental data are different than those of the mixed solution and once all the possible θ values are taken into account in the 3-dimensional BK equation, the solution might result in an improved data agreement.

Chapter 7

Conclusions

Within this work, the state-of-the-art framework for studying a hadron structure was presented. The main focus on the explanation of the parton saturation phenomenon, its theoretical background and the numerical solution of emergent evolution equations.

After the general introduction in Chapter 1, a brief introduction to the experimental processes examined to study the hadron structure was given in Chapter 2. The scattering of an electron (or a positron) with a proton was described in greater detail with focus on the deep-inelastic regime. The connection between the theoretical formulas describing the collision experiments and a phenomenological interpretation of the proton composition was presented in the form of the proton structure functions within the parton model framework. A brief description of the model was given, followed by a discussion of its limitations, namely the low-x behaviour of the BFKL evolution equation. Confronted with theoretical restrictions following from higher physical principles such as unitarity, the parton model was shown to be insufficient. Namely, the absence and desirability of the so-called parton saturation mechanism was explained.

Subsequently, an alternative approach to the description of the scattering process was presented in the form of the colour dipole model in Chapter 3. In this picture, the interaction-mediating photon is expanded in its Fock space and the leading strongly interacting contribution (a dipole formed by a quark-antiquark pair) is taken to interact with a proton. The probability of such a process is encoded in the so-called dipole scattering amplitude.

To approach and overcome the parton model limitations, the more complex effective theory of the Colour Glass Condensate model was presented in Chapter 4. Its main ideas were described briefly, including the emergence of the JIMWLK evolution equations, moving directly to their limit case and the main topic of this work: the Balitsky-Kovchegov equation. This integro-differential equation describes the dipole scattering amplitude of the colour dipole model and its evolution with rapidity or equivalently, the Bjorken x.

The linear terms in the BK equation can be phenomenologically interpreted as an annihilation of the original dipole[1], while creating two new so-called daughter dipoles. It was remarked that the linear part is equivalent to the BFKL equation. Unlike the BFKL equation, the BK evolution contains an extra non-linear term. This can be interpreted as a recombination of the daughter dipoles at high densities, effectively incorporating the aforementioned saturation mechanism. A qualitative comparison of the different effects of the BFKL and the BK evolution equations was shown in Fig. 5.4.

The main goal of the thesis was to present a numerical solution of the BK equation. A solution in all four dimensions of the dipole scattering amplitude has not yet been achieved, however the one-dimensional and the state-of-the-art two-dimensional solutions were presented in Chapter 5. The 2-dimensional calculation was conducted for two exemplary values of the angle θ as a preview of the 3-dimensional solution. A full solution of the BK equation in its full spatial dependence is the objective of work following this thesis.

Overall, the Balitsky-Kovchegov equation was described in great detail, focusing on the role of its kernel and the initial condition needed for its solution. Their various combinations were used in the calculations to discuss their advantages and limitations.

In Fig. 5.1, the stability of the numerical solution is shown since even a very simple initial condition[2] leads to the same final shape of the dipole scattering amplitude, as in case of the initial conditions from the GBW and MV models. In the 1-dimensional solution driven by the running coupling, both physically motivated initial conditions resulted in a very similar solution as shown in Fig. 5.1. The prediction of the F_2 structure function in Fig. 6.1 also showed no major difference and only the MV was chosen to be used for the remaining prediction of the reduced DIS cross section in Fig. 6.3. All the predictions were compared with the combined experimental results of the H1 and ZEUS collaborations from the positron–proton collisions at HERA.

To solve the 2-dimensional BK equation, the MV initial condition was extended by the impact-parameter dependence as described by Eq. (4.15). The subsequent solution with the running coupling kernel exhibited a fast increase of the dipole scattering amplitude with rapidity, caused by the so-called Coulomb tails. Their presence in the BK equation solution was shown in Fig. 5.6. In order to curb their effect, the collinearly improved kernel was presented in Eq. (4.9). The resulting improvement of the solution is shown in Fig. 5.6 and Fig. 5.7. Ultimately, the resulting prediction of the F_2 structure function is shown in Fig. 6.2, comparing the effects of both kernels. The significant disagreement between the experimental data and the prediction

[1]Emergent form the photon which mediates the $e^{\pm} - p$ interaction.

[2]The Heaviside function modified such that not even its range corresponds to the evolution-given function.

obtained using the running coupling kernel is emphasized. Besides the mixed[3] 2-dimensional solution, the solution with $\theta = \frac{\pi}{2}$ was also used to calculate the reduced cross section as shown in Fig. 6.4, which served as another preview of the potential of a 3-dimensional solution.

Considering the number of approximations made on the way to derive the CGC effective theory and the BK equation together with the fact that the full-dimensional solution is not yet available, all the presented predictions of the observable quantities agree with the experimental data to a sufficient extent, suggesting the potential quality of the model. The most important steps to be further conducted are achieving the full-dimensional BK equation solution and fitting the necessary parameters to provide predictions of the observables.

[3]See Chapter 5.

Appendix A

The fourth-order Runge-Kutta method and the BK equation

Given an ordinary first-order differential equation

$$\frac{\mathtt{d}y(x)}{\mathtt{d}x} = f(x, y(x)), \tag{A.1}$$

the classical (fourth-order) Runge-Kutta method [50] can be used to obtain a numerical solution. The prescription reads

$$y(x+h) = y(x) + \frac{1}{6}k_1 + \frac{1}{3}k_2 + \frac{1}{3}k_3 + \frac{1}{6}k_4 + \mathcal{O}(h^2), \tag{A.2}$$

where the coefficients k_j are

$$k_1 = hf\left(x, y\right), \tag{A.3}$$

$$k_2 = hf\left(x + \frac{1}{2}h, y + \frac{1}{2}k_1\right), \tag{A.4}$$

$$k_3 = hf\left(x + \frac{1}{2}h, y + \frac{1}{2}k_2\right), \tag{A.5}$$

$$k_4 = hf\left(x + h, y + k_3\right). \tag{A.6}$$

To tailor the prescription to the BK equation, we take $f(x) \equiv N(\vec{r}, \vec{b}, Y)$ and the right-hand side f is identified with

$$\begin{aligned} f\left(N(\vec{r}, \vec{b}, Y)\right) &= \int \mathcal{D}K \Big[N(\vec{r}_1, \vec{b}_1, Y) + N(\vec{r}_2, \vec{b}_2, Y) - N(\vec{r}, \vec{b}, Y) \\ &\qquad N(\vec{r}_1, \vec{b}_1, Y) N(\vec{r}_2, \vec{b}_2, Y) \Big] \\ &= I_1 - N(\vec{r}, \vec{b}, Y) I_0 - I_2 \end{aligned} \tag{A.7}$$

as described at the beginning of Chapter 5.

Now since the BK equation right-hand side does not explicitly depend on Y, the x-terms in Eq. (A.6) disappear and we get

$$k_1 = hf\,(N) = h\bigg(I_1 - N(\vec{r},\vec{b},Y)I_0 - I_2\bigg) \tag{A.8}$$

$$\begin{aligned} k_2 = hf\left(N+\frac{k_1}{2}\right) &= h\int \mathcal{D}K\bigg[N(\vec{r}_1,\vec{b}_1,Y) + \frac{k_1}{2} + N(\vec{r}_2,\vec{b}_2,Y) + \cancel{\frac{k_1}{2}} \\ &\quad - N(\vec{r},\vec{b},Y) - \cancel{\frac{k_1}{2}} - \left(N(\vec{r}_1,\vec{b}_1,Y)+\frac{k_1}{2}\right)\left(N(\vec{r}_2,\vec{b}_2,Y)+\frac{k_1}{2}\right)\bigg] \\ &= h\int \mathcal{D}K\bigg[N(\vec{r}_1,\vec{b}_1,Y) + N(\vec{r}_2,\vec{b}_2,Y) - N(\vec{r},\vec{b},Y) - N(\vec{r}_1,\vec{b}_1,Y)N(\vec{r}_2,\vec{b}_2,Y) \\ &\quad + \frac{k_1}{2} - \frac{k_1}{2}\bigg(N(\vec{r}_1,\vec{b}_1,Y)+N(\vec{r}_2,\vec{b}_2,Y)\bigg) + \frac{k_1^2}{4}\bigg] = k_1 - h\bigg(\frac{k_1}{2}(I_0-I_1) + \frac{k_1^2}{4}I_0\bigg) \end{aligned} \tag{A.9}$$

$$\begin{aligned} k_3 = hf\left(N+\frac{k_2}{2}\right) &= h\int \mathcal{D}K\bigg[N(\vec{r}_1,\vec{b}_1,Y) + \frac{k_2}{2} + N(\vec{r}_2,\vec{b}_2,Y) + \cancel{\frac{k_2}{2}} \\ &\quad - N(\vec{r},\vec{b},Y) - \cancel{\frac{k_2}{2}} - \left(N(\vec{r}_1,\vec{b}_1,Y)+\frac{k_2}{2}\right)\left(N(\vec{r}_2,\vec{b}_2,Y)+\frac{k_2}{2}\right)\bigg] \\ &= h\int \mathcal{D}K\bigg[N(\vec{r}_1,\vec{b}_1,Y) + N(\vec{r}_2,\vec{b}_2,Y) - N(\vec{r},\vec{b},Y) - N(\vec{r}_1,\vec{b}_1,Y)N(\vec{r}_2,\vec{b}_2,Y) \\ &\quad + \frac{k_2}{2} - \frac{k_2}{2}\bigg(N(\vec{r}_1,\vec{b}_1,Y)+N(\vec{r}_2,\vec{b}_2,Y)\bigg) + \frac{k_2^2}{4}\bigg] = k_1 - h\bigg(\frac{k_2}{2}(I_0-I_1) + \frac{k_2^2}{4}I_0\bigg) \end{aligned} \tag{A.10}$$

$$\begin{aligned} k_4 = hf\left(N+\frac{k_3}{2}\right) &= h\int \mathcal{D}K\bigg[N(\vec{r}_1,\vec{b}_1,Y) + \frac{k_3}{2} + N(\vec{r}_2,\vec{b}_2,Y) + \cancel{\frac{k_3}{2}} \\ &\quad - N(\vec{r},\vec{b},Y) - \cancel{\frac{k_3}{2}} - \left(N(\vec{r}_1,\vec{b}_1,Y)+\frac{k_3}{2}\right)\left(N(\vec{r}_2,\vec{b}_2,Y)+\frac{k_3}{2}\right)\bigg] \\ &= h\int \mathcal{D}K\bigg[N(\vec{r}_1,\vec{b}_1,Y) + N(\vec{r}_2,\vec{b}_2,Y) - N(\vec{r},\vec{b},Y) - N(\vec{r}_1,\vec{b}_1,Y)N(\vec{r}_2,\vec{b}_2,Y) \\ &\quad + \frac{k_3}{2} - \frac{k_3}{2}\bigg(N(\vec{r}_1,\vec{b}_1,Y)+N(\vec{r}_2,\vec{b}_2,Y)\bigg) + \frac{k_3^2}{4}\bigg] = k_1 - h\bigg(\frac{k_3}{2}(I_0-I_1) + \frac{k_3^2}{4}I_0\bigg) \end{aligned} \tag{A.11}$$

as written in Eq. (5.12). The last step in each of the equations can be done since the k_j are already integrated over the measure $\mathcal{D}K$ and therefore do not depend on r_1 anymore.

Appendix B

The logarithmic Simpson's integration method

One of the assumptions when using the Simpson's integration method is that the interval is split into an even number n of equidistant[1] intervals of length h. However, the grid in the integration variable r_1 is logarithmic so a modification must be made.

An integral of a function f with of logarithmically sampled variable x can be rewritten by transition to a new variable

$$\xi = \log_{10} x = e^{x \ln 10} \quad \rightarrow \quad \mathtt{d}x = \ln(10) 10^{\xi} \mathtt{d}\xi, \tag{B.1}$$

so

$$\begin{aligned}
\int_{x_0}^{x_n} \mathtt{d}x f(x) &= \int_{10^{\xi_0}}^{10^{\xi_n}} \mathtt{d}\xi \ln(10) 10^{\xi} f(\xi) \\
&\stackrel{1}{=} \ln(10) \frac{10^{\xi_n} - 10^{\xi_0}}{3n} \Bigg[10^{\xi_0} f(10^{\xi_0}) + 2 \sum_{j=1}^{n/2-1} 10^{\xi_{2j}} f(10^{\xi_{2j}}) \\
&\qquad + 4 \sum_{j=1}^{n/2} 10^{\xi_{2j-1}} f(10^{\xi_{2j-1}}) + 10^{\xi_n} f(10^{\xi_n}) \Bigg] + \mathcal{O}(\frac{1}{n^4}) \\
&= \ln(10) \frac{x_n - x_0}{3n} \Bigg[x_0 f(x_0) + 2 \sum_{j=1}^{n/2-1} x_{2j} f(x_{2j}) \\
&\qquad + 4 \sum_{j=1}^{n/2} x_{2j-1} f(x_{2j-1}) + x_n f(x_n) \Bigg] + \mathcal{O}(\frac{1}{n^4})
\end{aligned} \tag{B.2}$$

[1] To be precise, the Simpson's method is also formulated for unevenly sampled data, however, in case of the logarithmic sampling a simpler method can be utilised, as shown here.

In step 1, the standard Simpson's formula could have been used as the integral was expressed with respect to the equidistantly sampled variable ξ

$$h = \xi_{n+1} - \xi_n \quad \forall n \in \mathbb{N}_0 \quad \rightarrow \quad x_{n+1} - x_n = 10^h x_n - x_n. \tag{B.3}$$

This corresponds exactly to the sampling of r_1 described in Eq. (5.21), hence the final form of Eq. (5.17).

Appendix C

The geometric layout and impact parameters

To show specifically, how the values of the impact parameters b_1 and b_2 are obtained, an extended version of Fig. 4.2 is presented in Fig. C.1.

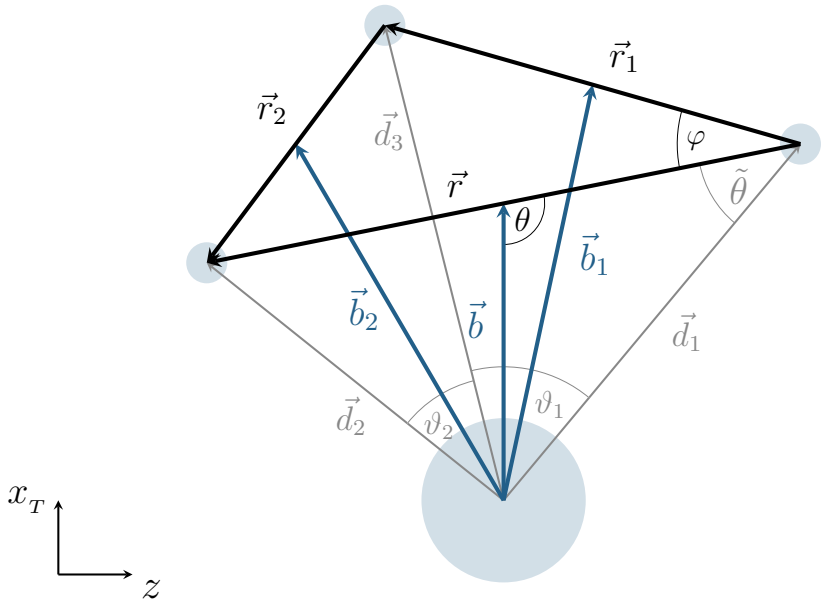

Fig. C.1: The proton-dipole interaction geometry in the z, x_T plane (rotational symmetry of the problem is assumed with respect to the z-axis). The large blue sphere represents the proton, the small spheres depict the dipole and an emergent gluon in correspondence to Fig. 4.1. The vector $\vec{b}$ denotes the original dipole impact parameter, $\vec{b_j}$ is an impact parameter of the j-th daughter dipole.

Firstly, the squared norms of the quark and antiquark positions vectors $d_{1,2}^2$ are simply

$$d_1^2 = \left|\vec{b} - \frac{\vec{r}}{2}\right|^2 = b^2 + \frac{r^2}{4} - rb\cos(\theta), \tag{C.1}$$

$$d_2^2 = \left|\vec{b} + \frac{\vec{r}}{2}\right|^2 = b^2 + \frac{r^2}{4} + rb\cos(\theta). \tag{C.2}$$

Secondly, let us express the square of $\vec{d_3} = \vec{d_1} + \vec{r_1}$

$$d_3^2 = d_1^2 + r_1^2 + 2r_1 d_1 \cos(\pi - \tilde{\theta} - \varphi) = d_1^2 + r_1^2 - 2r_1 d_1 \cos(\tilde{\theta} + \varphi), \tag{C.3}$$

where the angle $\tilde{\theta} = \arcsin\left(\frac{b}{d_1}\sin(\theta)\right)$ is obtained from the law of sines.

Finally, the squared sizes of the daughter-dipole impact parameters $b_{1,2}^2$ are calculated as

$$b_{1,2}^2 = \left|\frac{1}{2}\left(\vec{d_3} + \vec{d}_{1,2}\right)\right|^2 = \frac{1}{4}\left(d_3^2 + d_{1,2}^2 + 2d_3 d_{1,2}\cos(\vartheta_{1,2})\right) = \frac{1}{4}\left(2d_3^2 + 2d_{1,2}^2 - r_{1,2}^2\right), \tag{C.4}$$

where the last step uses that

$$r_{1,2}^2 = \left|\vec{d_3} - \vec{d}_{1,2}\right|^2 = d_3^2 + d_{1,2}^2 - 2d_3 d_{1,2}\cos(\vartheta_{1,2}). \tag{C.5}$$

Bibliography

[1] Planck Collaboration et al. *Planck 2018 results. VI. Cosmological parameters*. July 2018.

[2] E. Rutherford. "Collision of α particles with light atoms. IV. An anomalous effect in nitrogen". In: *Phil. Mag. Ser. 6* 37 (1919), pp. 581–587. DOI: 10.1080/14786431003659230.

[3] F. E. Close. *An Introduction to Quarks and Partons*. 1979. ISBN: 978-0-12-175152-4.

[4] Daniel Dominguez. "An artist's impression of the mayhem of quarks and gluons inside the proton." In: (June 2019). General Photo. URL: https://cds.cern.ch/record/2678286.

[5] A Cooper-Sarkar. "The structure of the proton as a function of scale, Q2, and fractional momentum, x." In: (May 2019). ISSN: 0304-288X. URL: https://cerncourier.com/wp-content/uploads/2019/07/CERNCourier2019MayJun-digitaledition.pdf.

[6] Richard P. Feynman. "Very High-Energy Collisions of Hadrons". In: *Phys. Rev. Lett.* 23 (24 Dec. 1969), pp. 1415–1417. DOI: 10.1103/PhysRevLett.23.1415. URL: https://link.aps.org/doi/10.1103/PhysRevLett.23.1415.

[7] Oscar Wallace Greenberg. "Parton Model". en. In: *Compendium of Quantum Physics*. Ed. by Daniel Greenberger, Klaus Hentschel, and Friedel Weinert. Berlin, Heidelberg: Springer Berlin Heidelberg, 2009, pp. 465–468. ISBN: 9783540706229 9783540706267. DOI: 10.1007/978-3-540-70626-7_139. URL: http://link.springer.com/10.1007/978-3-540-70626-7_139.

[8] F. Halzen and Alan D. Martin. *QUARKS AND LEPTONS: AN INTRODUCTORY COURSE IN MODERN PARTICLE PHYSICS*. 1984. ISBN: 978-0-471-88741-6.

[9] Robin Devenish. *Deep inelastic scattering*. Oxford New York: Oxford University Press, 2004. ISBN: 978-0-19-850671-3.

[10] B. Foster. "Deep Inelastic Scattering at HERA". In: *International Journal of Modern Physics A* 13.10 (Apr. 1998), pp. 1543–1621. ISSN: 1793-656X. DOI: 10.1142/s0217751x9800069x. URL: http://dx.doi.org/10.1142/S0217751X9800069X.

[11] A Baltz et al. "The physics of ultraperipheral collisions at the LHC". In: *Physics Reports* 458.1-3 (), pp. 1–171. ISSN: 0370-1573. DOI: 10.1016/j.physrep.2007.12.001. URL: http://dx.doi.org/10.1016/j.physrep.2007.12.001.

[12] Mark Thomson. *Modern particle physics*. New York: Cambridge University Press, 2013. ISBN: 978-1-107-03426-6.

[13] Matthew Schwartz. *Quantum field theory and the standard model*. Cambridge, United Kingdom New York: Cambridge University Press, 2014. ISBN: 978-1-107-03473-0.

[14] David Griffiths. *Introduction to elementary particles*. 2008. ISBN: 978-3-527-40601-2.

[15] M. Tanabashi et al. "Review of Particle Physics". In: *Phys. Rev. D* 98 (3 Aug. 2018), p. 030001. DOI: 10.1103/PhysRevD.98.030001. URL: https://link.aps.org/doi/10.1103/PhysRevD.98.030001.

[16] Michael Kuhlen. "QCD and the Hadronic Final State in Deep Inelastic Scattering at HERA". Other thesis. Dec. 1997. arXiv: hep-ph/9712505.

[17] Jamal Jalilian-Marian et al. "The BFKL equation from the Wilson renormalization group". In: *Nuclear Physics B* 504.1-2 (Oct. 1997), pp. 415–431. ISSN: 0550-3213. DOI: 10.1016/s0550-3213(97)00440-9. URL: http://dx.doi.org/10.1016/S0550-3213(97)00440-9.

[18] K Golec-Biernat. *Saturation effects in DIS at low x*. 2002. arXiv: 0207188 [hep-ph]. URL: https://arxiv.org/pdf/hep-ph/0207188.pdf.

[19] K. Golec-Biernat and M. Wüsthoff. "Saturation effects in deep inelastic scattering at low Q2 and its implications on diffraction". In: *Physical Review D* 59.1 (Nov. 1998). ISSN: 1089-4918. DOI: 10.1103/physrevd.59.014017. URL: http://dx.doi.org/10.1103/PhysRevD.59.014017.

[20] H. Kowalski, L. Motyka, and G. Watt. "Exclusive diffractive processes at HERA within the dipole picture". In: *Physical Review D* 74.7 (Oct. 2006). ISSN: 1550-2368. DOI: 10.1103/physrevd.74.074016. URL: http://dx.doi.org/10.1103/PhysRevD.74.074016.

[21] Dieter Schildknecht. "The color dipole picture". In: (2013). DOI: 10.1063/1.4802179. URL: http://dx.doi.org/10.1063/1.4802179.

[22] Javier L. Albacete et al. "AAMQS: A non-linear QCD analysis of new HERA data at small-x including heavy quarks". In: *The European Physical Journal C* 71.7 (July 2011). ISSN: 1434-6052. DOI: 10.1140/epjc/s10052-011-1705-3. URL: http://dx.doi.org/10.1140/epjc/s10052-011-1705-3.

[23] Cheuk-Yin Wong. *Introduction to High-Energy Heavy-Ion Collisions*. WORLD SCIENTIFIC, 1994. DOI: 10.1142/1128. eprint: https://www.worldscientific.com/doi/pdf/10.1142/1128. URL: https://www.worldscientific.com/doi/abs/10.1142/1128.

[24] Heikki Mäntysaari. *Scattering off the Color Glass Condensate*. 2015. arXiv: 1506.07313 [hep-ph].

[25] Heikki Mäntysaari. *Balitsky-Kovchegov equation*. 2011. URL: http://urn.fi/URN:NBN:fi:jyu-2011121611810.

[26] Jan Cepila and Jesús Guillermo Contreras. *Rapidity dependence of saturation in inclusive HERA data with the rcBK equation*. 2016. arXiv: 1501.06687 [hep-ph].

[27] F. D. Aaron et al. "Combined measurement and QCD analysis of the inclusive $e^{\pm}p$ scattering cross sections at HERA". In: *Journal of High Energy Physics* 2010.1 (Jan. 2010). ISSN: 1029-8479. DOI: 10.1007/jhep01(2010)109. URL: http://dx.doi.org/10.1007/JHEP01(2010)109.

[28] H1 and ZEUS Collaborations. *Combination of Measurements of Inclusive Deep Inelastic $e^{\pm}p$ Scattering Cross Sections and QCD Analysis of HERA Data*. 2015. arXiv: 1506.06042 [hep-ex].

[29] Amir H. Rezaeian and Ivan Schmidt. "Impact-parameter dependent color glass condensate dipole model and new combined HERA data". In: *Physical Review D* 88.7 (Oct. 2013). ISSN: 1550-2368. DOI: 10.1103/physrevd.88.074016. URL: http://dx.doi.org/10.1103/PhysRevD.88.074016.

[30] Yuri V. Kovchegov and Eugene Levin. *Quantum Chromodynamics at High Energy*. Cambridge Monographs on Particle Physics, Nuclear Physics and Cosmology. Cambridge University Press, 2012. DOI: 10.1017/CBO9781139022187.

[31] Carlos Contreras, Eugene Levin, and Rodrigo Meneses. "BFKL equation in the next-to-leading order: solution at large impact parameters". In: *The European Physical Journal C* 79.10 (Oct. 2019). ISSN: 1434-6052. DOI: 10.1140/epjc/s10052-019-7363-6. URL: http://dx.doi.org/10.1140/epjc/s10052-019-7363-6.

[32] I. Balitsky. "Operator expansion for high-energy scattering". In: *Nuclear Physics B* 463.1 (Mar. 1996), pp. 99–157. ISSN: 0550-3213. DOI: 10.1016/0550-3213(95)00638-9. URL: http://dx.doi.org/10.1016/0550-3213(95)00638-9.

[33] Yuri V. Kovchegov. "Small-x F2 structure function of a nucleus including multiple Pomeron exchanges". In: *Physical Review D* 60.3 (June 1999). ISSN: 1089-4918. DOI: 10.1103/physrevd.60.034008. URL: http://dx.doi.org/10.1103/PhysRevD.60.034008.

[34] Yuri V. Kovchegov. "Unitarization of the BFKL Pomeron on a nucleus". In: *Physical Review D* 61.7 (Mar. 2000). ISSN: 1089-4918. DOI: 10.1103/physrevd.61.074018. URL: http://dx.doi.org/10.1103/PhysRevD.61.074018.

[35] Ian Balitsky. "Quark contribution to the small-x evolution of color dipole". In: *Physical Review D* 75.1 (Jan. 2007). ISSN: 1550-2368. DOI: 10.1103/physrevd.75.014001. URL: http://dx.doi.org/10.1103/PhysRevD.75.014001.

[36] Yuri V. Kovchegov and Heribert Weigert. "Triumvirate of running couplings in small-x evolution". In: *Nuclear Physics A* 784.1-4 (Mar. 2007), pp. 188–226. ISSN: 0375-9474. DOI: 10.1016/j.nuclphysa.2006.10.075. URL: http://dx.doi.org/10.1016/j.nuclphysa.2006.10.075.

[37] Edmond Iancu and Raju Venugopalan. "The Color Glass Condensate and High Energy Scattering in QCD". In: *Quark–Gluon Plasma 3* (Jan. 2004), pp. 249–363. DOI: 10.1142/9789812795533_0005. URL: http://dx.doi.org/10.1142/9789812795533%5C_0005.

[38] H Weigert. "Evolution at small x: The color glass condensate". In: *Progress in Particle and Nuclear Physics* 55.2 (Oct. 2005), pp. 461–565. ISSN: 0146-6410. DOI: 10.1016/j.ppnp.2005.01.029. URL: http://dx.doi.org/10.1016/j.ppnp.2005.01.029.

[39] Larry McLerran. "The CGC and the Glasma: Two Lectures at the Yukawa Institute". In: *Progress of Theoretical Physics Supplement* 187 (2011), pp. 17–30. ISSN: 0375-9687. DOI: 10.1143/ptps.187.17. URL: http://dx.doi.org/10.1143/PTPS.187.17.

[40] R Venugopalan. "The Color Glass Condensate: A summary of key ideas and recent developments". In: 48 (Jan. 2004). ISSN: 0146-6410. URL: https://arxiv.org/pdf/hep-ph/0412396.pdf.

[41] Raju Venugopalan. "Introduction to light cone field theory and high energy scattering". In: *Lecture Notes in Physics* (), pp. 89–112. DOI: 10.1007/bfb0107312. URL: http://dx.doi.org/10.1007/BFb0107312.

[42] A.H. Mueller. "A simple derivation of the JIMWLK equation". In: *Physics Letters B* 523.3-4 (Dec. 2001), pp. 243–248. ISSN: 0370-2693. DOI: 10.1016/s0370-2693(01)01343-0. URL: http://dx.doi.org/10.1016/S0370-2693(01)01343-0.

[43] Elena Ferreiro et al. "Nonlinear gluon evolution in the color glass condensate: II". In: *Nuclear Physics A* 703.1-2 (May 2002), pp. 489–538. ISSN: 0375-9474. DOI: 10.1016/s0375-9474(01)01329-x. URL: http://dx.doi.org/10.1016/S0375-9474(01)01329-X.

[44] J.L. Albacete and C. Marquet. "Gluon saturation and initial conditions for relativistic heavy ion collisions". In: *Progress in Particle and Nuclear Physics* 76 (May 2014), pp. 1–42. ISSN: 0146-6410. DOI: 10.1016/j.ppnp.2014.01.004. URL: http://dx.doi.org/10.1016/j.ppnp.2014.01.004.

[45] J. Cepila, J. G. Contreras, and M. Matas. "Collinearly improved kernel suppresses Coulomb tails in the impact-parameter dependent Balitsky-Kovchegov evolution". In: *Physical Review D* 99.5 (Mar. 2019). ISSN: 2470-0029. DOI: 10.1103/physrevd.99.051502. URL: http://dx.doi.org/10.1103/PhysRevD.99.051502.

[46] E. Iancu et al. "Resumming double logarithms in the QCD evolution of color dipoles". In: *Physics Letters B* 744 (May 2015), pp. 293–302. ISSN: 0370-2693. DOI: 10.1016/j.physletb.2015.03.068. URL: http://dx.doi.org/10.1016/j.physletb.2015.03.068.

[47] E. Iancu et al. "Collinearly-improved BK evolution meets the HERA data". In: *Physics Letters B* 750 (Nov. 2015), pp. 643–652. ISSN: 0370-2693. DOI: 10.1016/j.physletb.2015.09.071. URL: http://dx.doi.org/10.1016/j.physletb.2015.09.071.

[48] Larry McLerran and Raju Venugopalan. "Boost covariant gluon distributions in large nuclei". In: *Physics Letters B* 424.1-2 (Apr. 1998), pp. 15–24. ISSN: 0370-2693. DOI: 10.1016/s0370-2693(98)00214-7. URL: http://dx.doi.org/10.1016/S0370-2693(98)00214-7.

[49] D. Bendova et al. "Solution to the Balitsky-Kovchegov equation with the collinearly improved kernel including impact-parameter dependence". In: *Physical Review D* 100.5 (Sept. 2019). ISSN: 2470-0029. DOI: 10.1103/physrevd.100.054015. URL: http://dx.doi.org/10.1103/PhysRevD.100.054015.

[50] William Press. *Numerical recipes : the art of scientific computing*. Cambridge, UK New York: Cambridge University Press, 2007. ISBN: 978-0-511-33555-6.

[51] Richard Burden. *Numerical analysis*. Boston, MA: Cengage Learning, 2016. ISBN: 978-1-305-25366-7.

[52] Bhajan Grewal. *Numerical Methods in Engineering and Science : C, C++, and MATLAB*. Herndon, VA: Mercury Learning, 2019. ISBN: 978-1-68392-128-8.